Journal of Solid State Chemistry **143,** 182–197 (1999)
Article ID jssc.1999.8075, available online at http://www.idealibrary.com on IDEAL®

Characterization of Ternary Compounds in the $BaO:Fe_2O_3:TiO_2$ System: $Ba_6Fe_{45}Ti_{17}O_{106}$ and $BaFe_{11}Ti_3O_{23}$

T. A. Vanderah, W. Wong-Ng, B. H. Toby, V. M. Browning,† R. D. Shull, R. G. Geyer,* and R. S. Roth

*Materials Science and Engineering Laboratory, National Institute of Standards and Technology, Gaithersburg, Maryland 20899; *Electronics and Electrical Engineering Laboratory, National Institute of Standards and Technology, Boulder, Colorado 80303; and †Naval Research Laboratory, Washington, D.C. 20375*

Received June 11, 1998; in revised form October 13, 1998; accepted October 20, 1998

Single crystals of $Ba_6Fe_{45}Ti_{17}O_{106}$ and $BaFe_{11}Ti_3O_{23}$ were obtained as major and minor coproducts, respectively, by slow-cooling an off-stoichiometric $BaO:Fe_2O_3:TiO_2$ melt. The former compound exhibits variable stoichiometry, $Ba_6Fe_{48-x}Ti_{14+x}O_{106}$, with the Fe:Ti ratio dependent upon the partial pressure of oxygen. The value of x corresponds to the equivalents of reduction that occur to maintain electroneutrality as the Ti-content increases. When prepared in air, this phase occurs at $x = 3$ with the stoichiometry $Ba_6Fe_{45}Ti_{17}O_{106}$, while in 100% oxygen the x-value approaches zero with the resulting stoichiometry $Ba_6Fe_{48}Ti_{14}O_{106}$ (all Fe^{3+} and Ti^{4+}). The structures of $Ba_6Fe_{45}Ti_{17}O_{106}$ and $BaFe_{11}Ti_3O_{23}$ were solved using single-crystal X-ray diffraction methods. $Ba_6Fe_{45}Ti_{17}O_{106}$ was prepared in polycrystalline form, and further structural details, including accurate Fe/Ti occupancy factors, were determined by a combined refinement using neutron and synchrotron powder diffraction data. ($Ba_6Fe_{45}Ti_{17}O_{106}$: Space group $C2/m$ (No. 12); $a = 19.390(1)$ Å, $b = 20.260(1)$ Å, $c = 10.076(1)$ Å, $\beta = 105.27(1)^\circ$; $V = 3818.5(3)$ Å^3; $Z = 2$; $\rho_{calc} = 5.08$ g/cm^3. $Ba_6Fe_{11}Ti_3O_{23}$: Space group $C2/c$ (No. 15); $a = 19.561(1)$ Å, $b = 8.6614(7)$ Å, $c = 10.120(1)$ Å, $\beta = 105.62(1)^\circ$; $V = 1651.1(3)$ Å^3; $Z = 4$; $\rho_{calc} = 5.08$ g/cm^3.) Both compounds adopt eight-layer close-packed structures built from alternating *ccp* and *hcp* [O, (Ba, O)] layers stacked along the a-direction with a $(ch)_4$ repeat sequence. Both structures feature octahedral sites occupied by a mixture of Fe and Ti as well as tetrahedral sites occupied by Fe^{3+}; the structural formulas are $^{XII}Ba_6\ ^{IV}Fe_6\ ^{VI}(Fe_{39}Ti_{17})O_{106}$ and $^{XII}Ba\ ^{IV}Fe_2\ ^{VI}(Fe_9Ti_3)O_{23}$. Both compounds are partially reduced; the former contains 3 moles of Fe^{2+} (or Ti^{3+}) per formula unit, and the latter contains 1 mole. The formation of Fe^{2+} is considered more likely than Ti^{3+}, but could not be experimentally confirmed. $BaFe_{11}Ti_3O_{23}$ is apparently metastable in air when cooled from above the solidus and could not be prepared as a polycrystalline sample. Indexed experimental X-ray powder diffraction data for $Ba_6Fe_{45}Ti_{17}O_{106}$ are given. Polycrystalline samples of this compound were used to measure its magnetic and electrical properties. The magnetic behavior of $Ba_6Fe_{45}Ti_{17}O_{106}$ above room temperature up to 1073 K was found to obey the Curie–Weiss law, which indicated a small effective magnetic moment (34 μ_B per mole $Ba_6Fe_{45}Ti_{17}O_{106}$) and a large negative temperature intercept (− 806 K). Electrical resistivity measurements between room temperature and 120 K revealed nonmetallic behavior with an activation energy on the order of 0.17 eV. At 347 MHz under ambient conditions, $Ba_6Fe_{45}Ti_{17}O_{106}$ exhibited a relative permittivity of 24 and a dielectric loss tangent of 0.10. © 1999 Academic Press

INTRODUCTION

Ceramic magnetic oxides are used in essential components such as circulators and isolators in a wide variety of electronic applications for communication systems (1, 2). Desirable properties for these ceramics include high dielectric constant, low dielectric loss, and high saturation magnetization. A potential host for compounds with this set of properties is the $BaO:Fe_2O_3:TiO_2$ system, which was recently studied in order to evaluate the phase relations, crystal chemistry, and properties that occur between the technically important barium polytitanates and magnetic iron-containing oxides (3–5). The phase diagram study (3) confirmed the formation of at least 16 ternary phases in this system, the majority exhibiting new structural types. Included in this earlier report were the results of a preliminary single-crystal structural study of a phase with approximate stoichiometry $Ba_3Fe_{24}Ti_7O_{53}$ (deduced by assuming all Fe^{3+} and Ti^{4+}), referred to therein as phase "D" (3). Subsequently, another report appeared describing the crystal structure and magnetic properties of $Ba_3Fe_{24}Ti_7O_{53}$ (6), apparently the same phase "D" as reported in (3). The present report describes a complete structure determination of this phase using single-crystal X-ray combined with neutron and synchrotron powder diffraction methods. This compound is shown to occur in air at the stoichiometry $Ba_6Fe_{45}Ti_{17}O_{106}$, not $Ba_3Fe_{24}Ti_7O_{53}$ ($= Ba_6Fe_{48}Ti_{14}O_{106}$), as previously reported (3, 6). The results of magnetic,

0022-4596/99 $30.00

resistivity, and dielectric measurements of polycrystalline $Ba_6Fe_{45}Ti_{17}O_{106}$ are included. In addition, a single-crystal X-ray structure determination of the compound $BaFe_{11}Ti_3O_{23}$, which was obtained as a minor coproduct from a melt containing crystals of $Ba_6Fe_{45}Ti_{17}O_{106}$, is also described.

EXPERIMENTAL METHODS

Red-black single crystals of $Ba_6Fe_{45}Ti_{17}O_{106}$ and $BaFe_{11}Ti_3O_{23}$ were obtained as major and minor coproducts, respectively, by slow-cooling (3°C/h) an off-stoichiometric liquid ($BaO:Fe_2O_3:TiO_2 = 0.125:0.500:0.375$) contained in a platinum capsule (2.6 mm i.d., partly open to the air) from 1450 to 1270°C, followed by air-quenching. Crystals were mechanically harvested from dark prismatic chunks of the recrystallized reaction mass and were initially characterized by the precession camera method (Zr-filtered Mo$K\alpha$ radiation) to assess quality, approximate cell parameters, and space group prior to further structural study. X-ray powder diffraction analysis of a representative portion of the reaction mass indicated the presence of $Ba_6Fe_{45}Ti_{17}O_{106}$ and hollandite-type $Ba_x(Fe,Ti)_8O_{16}$ as the major phases. This observation, plus data from several other melting experiments with the same starting composition ($BaO:Fe_2O_3:TiO_2 = 0.125:0.500:0.375$), which is within 1 mol% of $Ba_6Fe_{45}Ti_{17}O_{106}$, indicates that the latter compound melts incongruently between 1375 and 1400°C.

Polycrystalline reddish brown $Ba_6Fe_{45}Ti_{17}O_{106}$ was prepared by solid-state reaction of stoichiometric quantities of reagent grade $BaCO_3$, Fe_2O_3, and phosphate-free TiO_2 in air. Prior to each heating, the sample was ground 15–20 min with an agate mortar and pestle, pelletized, and placed on a layer of same-composition sacrificial powder on an alumina combustion boat. After an initial 50-h calcine at 1000°C, the sample was soaked at 1265°C, passively cooled to 750°C, and then air-quenched on the bench top. For a 10-g sample, three 1-week heatings at 1265°C were required to reach equilibrium, which was assumed when no changes could be detected in the details of the X-ray powder diffraction patterns. Portions of the final product were pelletized and sintered at 1265°C for 1–3 days for dielectric, resistivity, and magnetic measurements. The second compound, $BaFe_{11}Ti_3O_{23}$, could not be prepared in air in polycrystalline form; its X-ray powder pattern, calculated from the results of the single-crystal study, was not observed during the determination of the subsolidus BaO–Fe_2O_3–TiO_2 phase diagram (in air, 1250–1275°C) (3).

Laboratory X-ray powder diffraction data were collected using a Philips[1] diffractometer equipped with incident soller slits, theta-compensating slits, a 0.2 mm receiving slit, a graphite monochromator, and a scintillation detector. Data were collected at ambient temperatures using Cu$K\alpha$ radiation with a 0.015° 2θ step size and a 3 s count time. The sample was mounted by side-drifting into a welled holder (0.75 mm deep) to minimize preferred orientation. Intensity data measured as relative peak heights above background of hand-picked peaks were obtained using the Siemens DIFFRAC5000 second derivative peak locate program. The observed 2θ line positions reported here have been corrected using SRM 660, LaB_6 (7), as an external calibrant. The unit cell was refined from the corrected powder diffraction data (2θ values; Cu$K\alpha_1 = 1.540562$ Å) using the least-squares program CELLSVD (8). During the refinement, the indices of 29 unequivocally indexed reflections were fixed in accordance with the powder pattern calculated using the GSAS package (9) and the positional parameters from the single-crystal X-ray study.

Structure determinations of both compounds were carried out by single-crystal X-ray diffraction. Data were obtained using a VAX3000-controlled four-circle diffractometer (CAD4) with graphite-monochromated Mo$K\alpha$ ($\lambda = 0.71073$ Å) radiation. Twenty-five reflections (range $28° < 2\theta < 40°$ for $Ba_6Fe_{45}Ti_{17}O_{106}$ and $28° < 2\theta < 44°$ for $BaFe_{11}Ti_3O_{23}$) were used for least-squares refinement of the cell parameters (10). The ω–2θ scan method was used for data collection to a maximum 2θ-angle of 70° for both compounds. Crystal stability and orientation were monitored using three strong reflections and three high-2θ reflections; no decay corrections were necessary. Intensities were corrected for Lorentz-polarization effects. Experimental absorption corrections were made using the ellipsoidal approach. Structural refinements were carried out on a P5-90 computer with the program suite SHELXTL (11). Atomic scattering factors were taken from the International Tables for Crystallography (12). Experimental details are collected in Table 1. Both structures were solved by direct methods (13). In both cases, one Ba atom was correctly obtained first, and the remaining atoms were located from subsequent difference Fourier syntheses. Structures were refined by full-matrix least-squares on F^2. Six-coordinated sites were assumed to be fully occupied by a mixture of Fe^{3+} and Ti^{4+}, which have similar ionic radii (14), and tetrahedral sites by Fe^{3+}. During the refinement, the thermal parameters of the mixed Fe/Ti sites were constrained to be equal. Since a polycrystalline sample could not be prepared for $BaFe_{11}$ Ti_3O_{23}, the Fe and Ti occupancies were refined using the single-crystal data in order to estimate the stoichiometry of the compound. The results of qualitative chemical analysis of a crystal of this phase (by scanning electron microscopy with energy dispersive X-ray spectrometry) were consistent with the stoichiometry thus obtained.

For $Ba_6Fe_{45}Ti_{17}O_{106}$, accurate Fe/Ti occupancies and bond distances were obtained by a combined refinement

[1] Certain commercial equipment is identified in order to adequately specify the experimental procedure; recommendation or endorsement by the National Institute of Standards and Technology is not therein implied.

TABLE 1
Summary of Experimental Parameters and Refinement Results from Single-Crystal X-Ray Diffraction Studies

	$Ba_6Fe_{45}Ti_{17}O_{106}$	$BaFe_{11}Ti_3O_{23}$
Color	Red-black	Red-black
Temperature	$\approx 25°C$	$\approx 25°C$
Radiation (graphite monochromator)	Mo, 0.71073 Å	Mo, 0.71073 Å
Crystal dimensions	$0.15 \times 0.11 \times 0.06$	$0.14 \times 0.09 \times 0.05$ mm
Space group	$C2/m$ (No.12)	$C2/c$ (No.15)
Unit cell[a]		
a	19.439(1) Å	19.561(1) Å
b	20.304(1) Å	8.6614(7) Å
c	10.088(1) Å	10.120(1) Å
β	105.36(3)°	105.62(1)°
Vol.	3839.2(3) Å^3	1651.1(3) Å^3
Z	2	4
ρ_{calc}	5.08 g/cm^3	5.08 g/cm^3
Standard reflections:		
Intensity monitor	(0 −14 0), (−9 7 −2), (−12 0 4)	(0 6 0) (16 0 0), (−3 −3 6)
Orientation monitor	(−1 −11 −7), (−16 0 0), (−5 −19 2)	(2 8 2), (−20 0 4), (−4 2 10)
Reflections measured:		
Total	4571	3278
Independent	4298	2857
refinement used ($F_o > 4\sigma$)	3172	2557
Max. 2θ	54°	64°
Range of hkl	$-24 < h < 0,\ -25 < k < 0,\ -12 < l < 12$	$-29 < h < 28,\ 0 < k < 12,\ 0 < l < 15$
Min./max. transmission	17.6 to 24.2%	14.5 to 25.2%
Absorption (ellipsoid)	13.11 mm^{-1}	12.78 mm^{-1}
$\delta\rho_{max}$	5.06 e/Å^3	9.45 e/Å^3
$\delta\rho_{min}$	−1.59 e/Å^3	−2.71 e/Å^3
Refinement on F^2:		
R ($F_o > 4\sigma F_o$)	0.035	0.055
wR (F^2)	0.08	0.138
	$w = 1/[\sigma^2 F_o^2 + (0.0370P)^2]$	$w = 1/[\sigma^2 F_o^2 + 0.0682P^2 + 83.97P]$
	where $P = (F_o^2 + 2F_c^2)/3$)	where $P = (F_o^2 + 2F_c^2)/3$
Extinction coefficient	6.7×10^{-4}	1.0×10^{-3}
GOF	1.07	1.08
Largest shift/error	0.00	0.00

[a] See Table 4 for refined unit cell dimensions from X-ray powder diffraction data.

[b] NAPS document No. 05500 for 70 pages of supplementary material. This is not a multiarticle document. Order from NAPS c/o Microfiche Publications, 248 Hempstead Turnpike, West Hempstead, New York, 11552. Remit in advance in U.S. funds only $40.00 for photocopies or $6.00 for microfiche. There is a $25.00 invoicing charge on all orders filled before payment. Outside U.S. and Canada, add postage of $4.50 for the first 20 pages and $1.00 for each 10 pages of material thereafter, or $5.00 for the first microfiche and $1.00 for each microfiche thereafter.

using neutron and synchrotron powder diffraction data. The single-crystal structural model was used as a starting point for this refinement. Neutron data were collected under ambient conditions with the 32 detector BT-1 diffractometer at the NBSR research reactor of the National Institute of Standards and Technology using a Cu(311) monochromator ($\lambda = 1.5396(1)$ Å). The sample was loaded in a 6-mm-diameter vanadium container. No attempt was made to detect magnetic scattering at low temperatures because of the highly complex crystal structure. Synchrotron diffraction data were collected under ambient conditions on the X7A instrument at the Brookhaven National Synchrotron Light Source. The sample was contained in a glass capillary tube (0.26 mm diameter) which was rotated continuously during data collection. An incident wavelength of 0.69992(4) Å was obtained using a channel-cut Ge(111) monochromator. Intensities were measured using the central 20 mm of a 100-mm Kr-filled PSD. The combined structural refinements were carried out using the GSAS software package (9). Each set of data was weighted by its counting statistics. The refined parameters included scale factor; background function (high-order polynominals); profile parameters U, V, W; asymmetry coefficient; lattice parameters; atomic coordinates; and isotropic temperature factors. The experimental parameters and final results are collected in Table 2. No impurity peaks were

TABLE 2
Summary of Experimental Parameters and Refinement Results from Neutron Diffraction and Synchrotron Radiation Studies of Polycrystalline $Ba_6Fe_{45}Ti_{17}O_{106}$

	Neutron	Synchrotron
Unit cell[a]		$a = 19.4119(4)$ Å $b = 20.2777(4)$ Å $c = 10.0831(2)$ Å $\beta = 105.2734(3)^\circ$ Vol. = 3828.8(2) Å^3
R_P (profile)	0.0460	0.0353
R_{wp} (weighted profile)	0.0537	0.0409
R_e (expected profile)	0.0487	0.0189
R_F^2 (Bragg)	0.0517	0.0398
Reduced χ^2		3.366
Total refined variables		195
Contribution to χ^2	15%	85%
λ	1.53960 Å	0.699919 Å
Minimum 2θ	5.05°	7.01°
Maximum 2θ	149.95°	49.99°
$2\theta_0$	−0.0288°	0.0172°
Number of reflections	4096	3629
Minimum d-spacing	0.797 Å	0.8258 Å
Maximum d-spacing	13.7572 Å	13.7572 Å
Max., min. Fourier values	0.097, −0.090 barn/A^3	2.2,-0.94 e/A^3
Profile function	Gaussian (with GSAS type 1 asymmetry correction)	Pseudo-Viogt (with Finger *et al.* [15] asymmetry correction)
Gaussian U, V, W	269, −293, 163	21.4, −8.76, 3.77
Cauchy X, Y	0.0, 0.0	0.66, 0.0
Background function	Chebyschev polynominal (16 coefficient)	Chebyschev polynominal (12 coefficient)

[a] See Table 4 for refined unit cell dimensions from X-ray powder diffraction data.

detectable in the diffraction data from the polycrystalline sample. During the refinements, the highly correlated atomic coordinates for each mixed Fe/Ti site were constrained to be the same. Temperature factors were grouped by atom type; i.e., single isotropic values were used for Ba, Fe/Ti, and O. Since the stoichiometry calculated from site multiplicities, assuming full occupancies and the presence of Fe^{3+} and Ti^{4+} (i.e., $Ba_6Fe_{48}Ti_{14}O_{106}$), was known to be inconsistent with the phase diagram determined from a large number of samples (3), trial refinements were carried out with the total occupancies of the transition metal sites unconstrained. No statistical improvements in the final results were obtained by assuming the presence of cation site vacancies. The final refinements were carried out assuming full site occupancies, with tetrahedral sites occupied exclusively by Fe^{3+}. The overall stoichiometry reported here, $Ba_6Fe_{45}Ti_{17}O_{106}$, was deduced by simultaneous consideration of the Fe/Ti occupancies from the neutron diffraction results and the phase diagram relations determined previously in air at 1250–1270°C (3). In that study, the disappearing phase method using X-ray powder diffraction data revealed no detectable solid solution behavior around $Ba_6Fe_{45}Ti_{17}O_{106}$.

Magnetic data for $Ba_6Fe_{45}Ti_{17}O_{106}$ below room temperature to 5 K were measured in helium using a SQUID magnetometer. For these measurements, the polycrystalline sample was immobilized by mixing with an epoxy which was cured at room temperature. All data were corrected for the small diamagnetic susceptibility of the epoxy ($\chi_g = -7.5 \times 10^{-9}$ m^3/kg at $T = 300$ K and $\chi_g = -5.2 \times 10^{-9}$ m^3/kg at $T = 5$ K) which had been measured in a separate experiment. Magnetic data above room temperature to 1073 K were measured in air using a sintered pellet of polycrystalline material and a vibrating sample magnetometer calibrated with a sample of high-purity nickel. The temperature dependence of the magnetization (at an applied field of 736 kA/m (9250 Oe)) was measured in two ways: (a) as the sample was cooled in the field from 1073 K (referred to as field-cooled, FC), and (b) as the sample was heated from room temperature after first heating to 1073 K and cooling to 300 K in zero field (referred to as zero-field-cooled, ZFC). For the measurements below 300 K, FC and ZFC refer to data obtained during cooling from room temperature in the applied field and data measured during heating after first cooling (at $H = 0$) to the lowest temperature, respectively.

Resistivity vs temperature data for a sintered polycrystalline disk of $Ba_6Fe_{45}Ti_{17}O_{106}$ were obtained using a conventional four-probe DC measurement technique. Resistivity was measured in vacuum between ambient temperature and $\sim$120 K using a closed-cycle refrigerator. The measuring current varied between 1 nA and 1 μA; below 120 K the resistivity became too large to measure.

Permittivity and dielectric loss tangent measurements of $Ba_6Fe_{45}Ti_{17}O_{106}$ at ambient temperature were carried out using a sintered disk of polycrystalline material, $\sim$11 mm in diameter, $\sim$1–2 mm thick, and approximately 75% dense. Measurements above 1 GHz using a resonator configuration (4) were precluded by the large dielectric loss ($\tan\delta > 10^{-3}$) exhibited by the sample. Therefore, dielectric properties were measured using a doubly reentrant cavity at lower frequencies. This method (16–20) permits the evaluation of permittivity and dielectric loss over a wide range of frequencies (100 MHz to 1 GHz) using relatively small, cylindrically shaped specimens. Accurate dielectric loss data can be obtained for low- to medium-loss materials ($\tan\delta \sim 10^{-1}$ to 10^{-3}). A schematic of the doubly reentrant cavity is shown in Fig. 1. The electric field structure in this arrangement is normal to the axial planar specimen surfaces; therefore, depolarization effects can occur that lead to underestimation of the intrinsic sample permittivity, and care must be taken to avoid air gaps between the specimen and the adjustable inner conductor of the cavity. Permittivity and dielectric loss tangent values were corrected to theoretical density using effective-medium formalisms for a two-phase composite (21, 22). The uncertainties in the reported values are approximately $\pm$10% and are dominated by the estimate of pore volume.

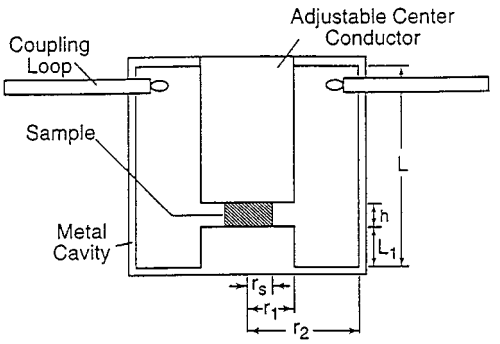

FIG. 1. Schematic diagram of the reentrant cavity used to measure permittivity and dielectric loss. The adjustable microwave coupling loops are shown. The real permittivity and dielectric loss tangent are evaluated from the measured frequency shift and change in the unloaded Q-factor of the dominant resonant mode, with and without sample insertion.

RESULTS AND DISCUSSION

1. *Crystal Chemistry and Stoichiometry of* $Ba_6Fe_{45}Ti_{17}O_{106}$

The single-crystal X-ray diffraction study confirmed that this compound crystallizes in space group $C2/m$ with the lattice parameters given in Table 1. Positional parameters and site occupancies from the combined refinement using neutron and synchrotron powder diffraction data are given in Table 3. The structure features 3 crystallographically distinct sites for Ba, 18 for the transition metals, and 33 for oxygen. As depicted in Fig. 2, $Ba_6Fe_{45}Ti_{17}O_{106}$ adopts a close-packed structure built from alternating *ccp* and *hcp* [O,(Ba, O)] layers stacked along the *a*-direction in an eight-layer (8L) $(ch)_4$ repeating sequence (23). All Ba ions are 12-coordinated, six Fe ions are 4-coordinated, and the remaining Fe and Ti cations are distributed among 6-coordinated sites, resulting in the structural formula $^{XII}Ba_6\ ^{IV}Fe_6\ ^{VI}(Fe_{39}Ti_{17})O_{106}$. The close-packed array does not contain vacancies as sometimes observed for complex barium titanate compounds (24–26). Within each of the eight *cp* layers, as illustrated in Fig. 3, the transition-metal polyhedra form "aesthetically pleasing" patterns reminiscent of those observed for the layered barium polytitanates (26). Within and between these layers the $[(Fe,Ti)O_6]$ octahedra are linked to each other by edges and vertices; no face-sharing occurs despite the presence of four *hcp* layers per unit cell. Half the layers contain $[FeO_4]$ tetrahedra, which are vertex-linked to $[(Fe,Ti)O_6]$ octahedra but not to each other. The indexed experimental X-ray powder diffraction pattern and refined unit cell for $Ba_6Fe_{45}Ti_{17}O_{106}$ are given in Table 4; the resulting figure of merit (27) is $F(132) = 8.6(0.012,869)$.

Bond distances, site distortion ratios, and bond valence sums (28) for $Ba_6Fe_{45}Ti_{17}O_{106}$ are collected in Table 5. All the polyhedra in the structure are somewhat distorted, as has generally been observed for compounds in this system (3–5, 29). The high bond valence sum of 2.38 v.u. observed for Ba1, which reflects short Ba1–O bond distances, suggests the presence of residual compressive strain at this site that is not relieved by distortion. Similarly high bond valence sums about Ba are fairly frequently observed in complex oxides (30), including other ternary compounds in this system (4, 5, 29). Brown and others (31–33) have described how such residual bond strain, if large enough, can affect physical properties and structural stability.

The bond valence sums given in Table 5 for the transition-metal sites in $Ba_6Fe_{45}Ti_{17}O_{106}$ were obtained by calculating a weighted average, using the Fe/Ti site occupancies determined by neutron diffraction (Table 3), and the formalism and parameters of Brese and O'Keeffe (28), and by initially assuming the oxidation states of Fe^{3+} and Ti^{4+}. The stoichiometry of the compound, however, requires three equivalents of reduction of either Fe^{3+} or Ti^{4+} to achieve electroneutrality. This reduction should cause an increase in (Fe/Ti)–O bond distances owing to the significantly larger sizes of Fe^{2+}/Ti^{3+} (14). Although the structure appears to contain some residual strain and is therefore

TABLE 3
Positional Parameters and Fe/Ti Site Occupancies for $Ba_6Fe_{45}Ti_{17}O_{106}$ from the Combined Refinement Using Neutron and Synchrotron Powder Diffraction Data

Atom	Site	x	y	z	Fe_{occ}/Ti_{occ}
Ba1	4*g*	0.5	0.2149(2)	0.0	
Ba2	4*i*	0.2388(2)	0.0	0.1254(3)	
Ba3	4*h*	0.5	0.3592(1)	−0.5	
M1	8*j*	0.4304(3)	0.3460(3)	−0.2107(5)	0.58(3)/0.42(3)
M2	8*j*	0.4346(3)	0.0785(2)	−0.1981(5)	0.83(3)/0.17(3)
M3	4*i*	0.5686(4)	0.5	−0.3250(7)	0.38(4)/0.62(4)
Fe4	4*i*	0.2785(3)	0.0	−0.2007(6)	1.0/0.0
M5	8*j*	0.3220(3)	0.1374(2)	0.0059(5)	0.58(3)/0.42(3)
M6	8*j*	0.3228(3)	0.2823(2)	−0.5131(5)	0.84(3)/0.16(3)
M7	4*i*	0.4293(4)	0.0	0.0514(8)	0.77(4)/0.23(4)
Fe8	8*j*	0.2804(2)	0.1473(2)	0.3109(5)	1.0/0/0
M9	8*j*	0.3179(3)	0.2057(2)	−0.2631(5)	0.90(3)/0.10(3)
M10	8*j*	0.3174(2)	0.2888(2)	−0.0190(5)	0.94(3)/0.06(3)
M11	8*j*	0.5656(3)	0.0710(2)	−0.3061(5)	0.53(3)/0.47(3)
M12	8*j*	0.3123(2)	0.4266(2)	−0.4957(5)	0.80(3)/0.20(3)
M13	8*j*	0.4309(3)	0.1485(3)	−0.4455(6)	0.55(3)/0.45(3)
M14	4*i*	0.4295(4)	0.5	−0.2217(7)	0.40(4)/0.60(4)
M15	8*j*	0.5692(3)	0.4224(3)	−0.0563(5)	0.60(4)/0.40(4)
M16	8*j*	0.3201(3)	0.3659(2)	0.2358(5)	0.77(3)/0.23(3)
M17	4*i*	0.3313(4)	0.0	−0.4995(8)	0.40(4)/0.60(4)
M18	8*j*	0.4356(3)	0.2272(2)	0.2854(5)	0.53(3)/0.47(3)
O1	8*j*	0.378(1)	0.1453(9)	−0.139(2)	
O2	2*a*	0.5	0.5	0.0	
O3	4*i*	0.613(1)	0.5	−0.113(3)	
O4	4*i*	0.380(1)	0.0	−0.148(3)	
O5	8*j*	0.255(1)	0.0717(9)	−0.614(2)	
O6	8*j*	0.373(1)	0.2833(9)	−0.152(2)	
O7	8*j*	0.3795(9)	0.2152(8)	0.104(2)	
O8	8*j*	0.502(1)	0.288(1)	0.246(2)	
O9	8*j*	0.628(1)	0.3569(9)	−0.101(2)	
O10	8*j*	0.371(1)	0.2098(8)	−0.396(2)	
O11	8*j*	0.494(1)	0.1453(9)	−0.261(2)	
O12	4*i*	0.505(1)	0.0	−0.242(3)	
O13	4*g*	0.5	0.065(1)	0.0	
O14	8*j*	0.381(1)	0.074(1)	−0.395(2)	
O15	4*i*	0.241(1)	0.0	−0.403(2)	
O16	4*i*	0.377(1)	0.0	0.349(3)	
O17	8*j*	0.257(1)	0.1441(9)	0.124(2)	
O18	8*j*	0.249(1)	0.2235(8)	−0.617(2)	
O19	8*j*	0.371(1)	0.3554(9)	−0.400(2)	
O20	8*j*	0.376(1)	0.0699(9)	0.105(2)	
O21	8*j*	0.502(1)	0.430(1)	−0.231(2)	
O22	4*i*	0.367(1)	0.500000	−0.392(3)	
O23	8*j*	0.237(1)	0.1473(9)	−0.362(2)	
O24	8*j*	0.382(1)	0.1517(8)	0.355(2)	
O25	8*j*	0.374(1)	0.2909(9)	0.341(2)	
O26	8*j*	0.258(1)	0.2089(8)	−0.111(2)	
O27	4*h*	0.5	0.079(1)	−0.5	
O28	8*j*	0.387(1)	0.4284(9)	−0.138(2)	
O29	4*h*	0.5	0.217(1)	0.5	
O30	4*g*	0.5	0.364(1)	0.0	
O31	2*c*	0.5	0.5	−0.5	
O32	8*j*	0.252(1)	0.0749(9)	−0.120(2)	
O33	8*j*	0.126(1)	0.0707(9)	−0.358(2)	

Note. *M* denotes a six-coordinated site with mixed Fe/Ti occupancy. Fe sites are four-coordinated. Temperature factors were grouped by atom type; single isotropic values were used for all Ba (0.40(3) Å^2); Fe,Ti (0.39(2) Å^2); and O (0.53(4) Å^2) sites.

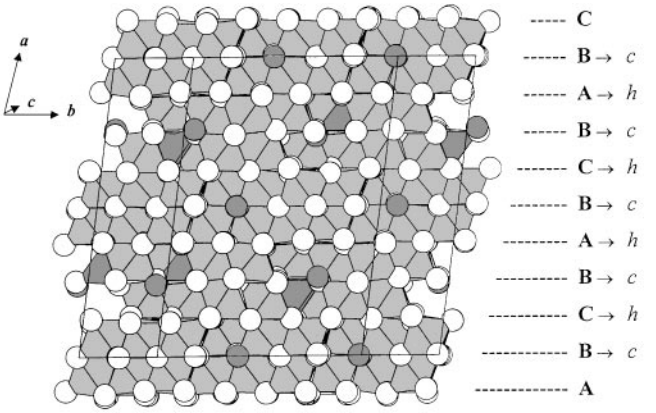

FIG. 2. The structure of $Ba_6Fe_{45}Ti_{17}O_{106}$ as viewed approximately along the *c*-direction, drawn (using the program ATOMS, Shape Software) to emphasize the stacking sequence of the close-packed [O,(Ba,O)] layers. Successive layers alternate between *ccp* and *hcp* along the a-axis, resulting in an 8L structure with a $(ch)_4$ repeat pattern. The structural formula for the compound is $^{XII}Ba_6{}^{IV}Fe_6{}^{VI}(Fe_{39}Ti_{17})O_{106}$. Shaded spheres denote Ba ions, white spheres are oxygens; the darker polyhedra depict $[FeO_4]$ tetrahedra while the lighter polyhedra represent the mixed $[(Fe,Ti)O_6]$ octahedral sites.

expected to deviate somewhat from the valence sum rule, inspection of Table 5 reveals anomalously low bond valence sums about *M*3, *M*11, and *M*17 that deviate 0.4–0.6 v.u. below that expected in the presence of Fe^{3+} and Ti^{4+}. Recalculation of the bond valence sums about these sites, assuming the presence of either Fe^{2+} or Ti^{3+}, results in significantly better agreement between observed and calculated values (i.e., BVS_{obs}/BVS_{calc} v.u. values, 1) assuming Fe^{2+}/Ti^{4+}: *M*3 = 3.15/ 3.24, *M*11 = 2.86/2.94, *M*17 = 2.95/ 3.20, or assuming Fe^{3+}/Ti^{3+}: *M*3 = 3.08/3.00, *M*11 = 2.86/ 3.00, *M*17 = 2.90/3.00). Furthermore, calculation of the equivalents of reduction (with either assumption) from the multiplicities of these sites results in a total that is approximately equal to that required for electroneutrality of the unit cell contents. These results are consistent with the presence of localized carriers in $Ba_6Fe_{45}Ti_{17}O_{106}$, which were known to be nonmetallic from preliminary resistivity measurements (3). Attempts to experimentally confirm the presence of $3Fe^{2+}$ per $Ba_6Fe_{45}Ti_{17}O_{106}$ formula unit using Mössbauer spectroscopy were not conclusive. Confirmation of which species is reduced may be experimentally intractable owing to the very small concentration of Fe^{2+} or Ti^{3+} (1.7 at%); however, a comparison of the observed redox behavior of Fe^{3+} and Ti^{4+} oxide systems suggests that reduction of Fe^{3+} to Fe^{2+} is thermodynamically more likely. For example, aqueous reduction potentials (34) indicate that one-equivalent Fe^{3+} reduction is considerably more favorable than that of Ti^{4+}. Furthermore, detailed phase equilibria stuies of iron titanium oxide mineral systems (35, 36) indicate that Ti^{4+} does not reduce to Ti^{3+}

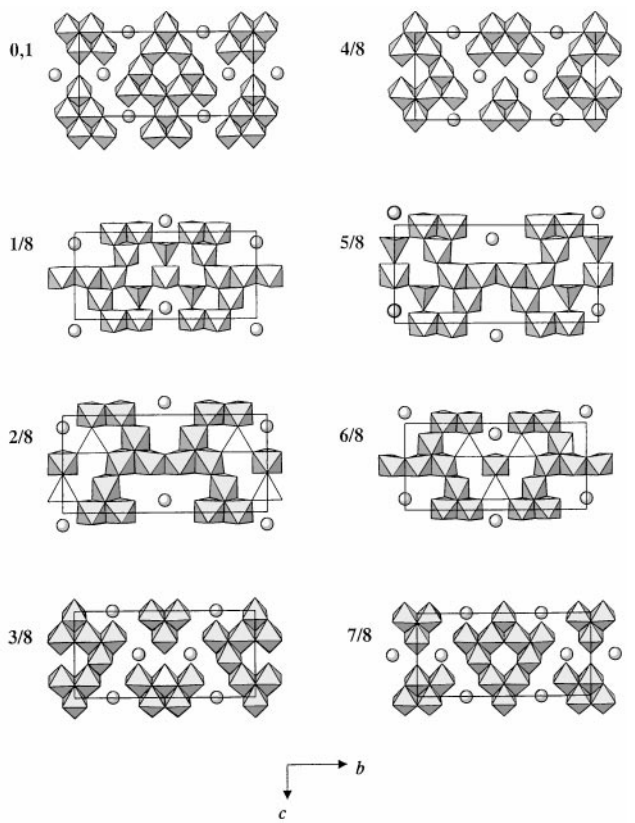

FIG. 3. Views of the polyhedral patterns formed within each of the eight close-packed (*cp*) layers of the $Ba_6Fe_{45}Ti_{17}O_{106}$ structure. The line of sight is perpendicular to the *bc*-plane which is parallel to the *cp* layers. Spheres denote Ba ions; oxygens are represented as polyhedral vertices. [(Fe,Ti)O_6] octahedra share edges and vertices within and beween the layers. Half of the layers contain [FeO_4] tetrahedra that are vertex-linked to [(Fe,Ti)O_6] octahedra but not to each other.

in the presence of Fe^{3+}, and that Fe^{3+} and Ti^{3+} are an "incompatible ion pair": in the ilmenite and ulvite systems studied, Ti^{3+} formed only after all Fe^{3+} had been reduced to Fe^{2+}.

The presence of a small amount of reduction in $Ba_6Fe_{45}Ti_{17}O_{106}$ suggested that this compound might exhibit variable stoichiometry depending on oxygen partial pressure. This was confirmed using a specimen that had been equilibrated in air (3) with the nominal overall composition $Ba_6Fe_{48}Ti_{14}O_{106}$, the stoichiometric analog of $Ba_6Fe_{45}Ti_{17}O_{106}$ with all Fe^{3+} and Ti^{4+}, which was the approximate composition initially reported (phase "D" (3)) from preliminary studies. This composition, as prepared in air at 1265°C, results in a two-phase mixture[2] and falls essentially

[2] Detailed X-ray powder diffraction analysis is required because of overlapping strong lines; however, using clearly discernible weaker high-angle lines in the $BaFe_{12}O_{19}$-type pattern, the mixture with nominal overall composition "$Ba_6Fe_{48}Ti_{14}O_{106}$," as prepared in air, is seen to contain ~80 mol% $Ba_6Fe_{45}Ti_{17}O_{106}$ plus ~20 mol% $BaFe_{10.8}Ti_{0.9}O_{19}$.

TABLE 4
X-Ray Powder Diffraction Data for $Ba_6Fe_{45}Ti_{17}O_{106}$ ($C2/m$: $a = 19.390(1)$ Å, $b = 20.260(1)$ Å, $c = 10.076(1)$ Å; $\beta = 105.27(1)^\circ$)

h	k	l	$2\theta_{obs}$	I_{obs}	$2\theta_{calc}$	$\Delta 2\theta$	d_{obs}
−1	3	1	15.987	2	15.957	0.030	5.5391
0	0	2	18.263	3	18.238	0.025	4.8536
4	0	0	18.986	3	18.963	0.023	4.6704
0	4	1	19.778	5	19.749	0.029	4.4851
2	4	0	19.940	2	19.919	0.021	4.4490
0	2	2	20.251	2	20.248	0.003	4.3814
4	2	0	20.890	5	20.906	−0.016	4.2488
1	5	0	22.447	1	22.432	0.015	3.9575
3	3	1	23.014	4	22.989	0.025	3.8613
1	3	2	24.029	1	24.010	0.019	3.7004
−4	2	2	24.312	1	24.295	0.017	3.6580
4	2	1	24.766	2	24.790	−0.024	3.5919
−4	4	1	25.770	4	25.754	0.016	3.4542
0	6	0	26.386	7	26.373	0.013	3.3749
0	0	3	27.503	1	27.505	−0.002	3.2404
−6	0	1	27.631	2	27.629	0.002	3.2256
−3	1	3	27.837	5	27.810	0.027	3.2022
0	6	1	27.964	7	27.949	0.015	3.1880
2	6	0	28.091	15	28.072	0.019	3.1739
2	4	2	28.825	9	28.814	0.011	3.0947
0	2	3	28.934	25	28.907	0.027	3.0833
3	5	1	29.056	36	29.035	0.021	3.0706
4	4	1	29.199	62	29.172	0.027	3.0559
−6	0	2	29.685	29	29.666	0.019	3.0070
1	5	2	29.883	37	29.863	0.020	2.9875
6	2	0			29.965		
−4	2	3	30.436	25	30.413	0.023	2.9344
5	3	1	30.767	12	30.747	0.020	2.9036
1	7	0	31.260	4	31.246	0.014	2.8589
−5	1	3	31.717	13	31.694	0.023	2.8188
−5	5	1	32.058	17	32.052	0.006	2.7896
0	6	2	32.266	4	32.255	0.011	2.7721
−7	1	1	32.598	14	32.603	−0.005	2.7446
2	2	3	32.749	9	32.732	0.017	2.7323
1	7	1	32.980	1	32.971	0.009	2.7137
6	2	1	33.586	18	33.577	0.009	2.6661
3	7	0	34.138	45	34.126	0.012	2.6242
−5	3	3			34.133		
3	5	2	34.277	20	34.277	0.000	2.6139
3	1	3	34.668	4	34.654	0.014	2.5853
−7	3	1	35.000	15	34.986	0.014	2.5615
0	8	0	35.417	9	35.416	0.001	2.5323
2	4	3	36.258	25	36.243	0.015	2.4755
5	3	2	36.438	3	36.432	0.006	2.4637
0	0	4			36.960		
−3	7	2	37.039	23	37.041	−0.002	2.4251
−2	8	1	37.296	5	37.277	0.019	2.4089
0	2	4	38.067	9	38.048	0.019	2.3619
2	8	1	38.554	2	38.559	−0.005	2.3332
−5	7	1	38.893	1	38.906	−0.013	2.3136
−4	6	3	39.640	1	39.656	−0.016	2.2717
4	8	0	40.455	5	40.474	−0.019	2.2278
−6	0	4	40.565	27	40.581	−0.016	2.2220
2	0	4			40.713		
−5	7	2	40.745	85	40.739	0.006	2.2126
3	7	2	40.817	78	40.805	0.012	2.2089

TABLE 4—*Continued*

h	k	l	$2\theta_{obs}$	I_{obs}	$2\theta_{calc}$	$\Delta 2\theta$	d_{obs}
3	5	3	41.135	1	41.130	0.005	2.1925
−8	4	1	41.265	1	41.269	−0.004	2.1859
5	1	3	41.608	7	41.608	0.000	2.1687
−1	5	4	42.503	5	42.511	−0.008	2.1251
−9	1	2	42.769	3	42.774	−0.005	2.1125
−6	6	3	43.725	0	43.723	0.002	2.0685
−9	3	1	44.152	2	44.140	0.012	2.0495
3	9	1	44.570	5	44.568	0.002	2.0312
−5	5	4	44.721	4	44.703	0.018	2.0247
1	9	2	45.141	6	45.145	−0.004	2.0068
−1	1	5	45.829	6	45.818	0.011	1.9783
−8	0	4	46.208	5	46.209	−0.001	1.9629
−7	7	2			46.366		
4	0	4	46.388	53	46.388	0.000	1.9557
−5	1	5	46.823	2	46.818	0.005	1.9386
5	9	0	47.093	3	47.076	0.017	1.9281
−9	3	3	47.221	6	47.230	−0.009	1.9232
2	10	1	47.320	5	47.321	−0.001	1.9194
2	8	3	48.114	5	48.107	0.007	1.8895
3	9	2	48.364	5	48.362	0.002	1.8804
−6	2	5	49.033	2	49.041	−0.008	1.8563
−3	9	3	49.194	2	49.216	−0.022	1.8506
10	2	0	49.506	3	49.514	−0.008	1.8396
1	9	3	50.273	6	50.277	−0.004	1.8133
−7	1	5	50.428	7	50.409	0.019	1.8081
4	10	1	50.933	13	50.927	0.006	1.7914
−9	3	4	51.521	3	51.530	−0.009	1.7723
−7	3	5	52.104	13	52.108	−0.004	1.7538
−2	10	3	52.765	1	52.776	−0.011	1.7334
−8	8	2	52.947	4	52.938	0.009	1.7279
−10	0	4	53.302	5	53.314	−0.012	1.7172
−9	7	2	53.455	68	53.469	−0.014	1.7127
6	0	4			53.528		
7	7	2			53.575		
3	7	4	54.145	14	54.154	−0.009	1.6924
−9	5	4	54.834	6	54.841	−0.007	1.6728
2	10	3	55.676	10	55.691	−0.015	1.6495
−8	4	5	55.917	9	55.927	−0.010	1.6429
6	10	1	56.235	4	56.248	−0.013	1.6344
−6	0	6	56.637	5	56.662	−0.025	1.6237
1	9	4	56.807	4	56.788	0.019	1.6193
−1	11	3	57.021	2	57.039	−0.018	1.6137
−5	3	6	57.303	1	57.301	0.002	1.6064
−6	2	6	57.459	6	57.452	0.007	1.6025
0	2	6	57.566	6	57.567	−0.001	1.5997
0	12	2	57.776	3	57.761	0.015	1.5944
3	5	5	57.866	5	57.883	−0.017	1.5921
−2	10	4	58.406	1	58.406	0.000	1.5787
−2	8	5	58.556	1	58.546	0.010	1.5750
4	4	5	58.887	3	58.887	0.000	1.5670
12	0	0	59.214	10	59.231	−0.017	1.5591
−9	9	1	59.390	4	59.371	0.019	1.5549
−5	11	3	59.729	5	59.739	−0.010	1.5469
−9	5	5	60.415	10	60.412	0.003	1.5309
−8	2	6	61.032	2	61.033	−0.001	1.5169
−12	0	4	61.586	25	61.595	−0.009	1.5046
−11	7	2	61.767	41	61.748	0.019	1.5006
8	0	4	61.827	55	61.839	−0.012	1.4993
9	7	2			61.870		
6	12	0	62.493	15	62.511	−0.018	1.4849

TABLE 4—*Continued*

h	k	l	$2\theta_{obs}$	I_{obs}	$2\theta_{calc}$	$\Delta 2\theta$	d_{obs}
4	6	5	62.666	7	62.683	−0.017	1.4812
−3	7	6	64.047	100	64.050	−0.003	1.4526
0	14	0	64.292	25	64.320	−0.028	1.4476
−5	13	1	64.476	7	64.454	0.022	1.4440
10	8	1	64.588	4	64.606	−0.018	1.4417
−8	8	5	65.068	2	65.072	−0.004	1.4322
−12	6	3	65.278	2	65.275	0.003	1.4281
7	9	3	65.518	2	65.520	−0.002	1.4235
−4	10	5	65.707	2	65.706	0.001	1.4198
−8	10	4	66.242	1	66.239	0.003	1.4097
−3	13	3	66.483	3	66.497	−0.014	1.4051
−2	12	4	66.628	5	66.629	−0.001	1.4024
−9	11	1	66.804	4	66.807	−0.003	1.3992
−9	5	6	67.242	8	67.259	−0.017	1.3911
3	5	6	67.442	11	67.469	−0.027	1.3875
12	0	2	67.722	5	67.740	−0.018	1.3824
−13	5	3	67.919	2	67.939	−0.020	1.3789
7	3	5	68.069	2	68.071	−0.002	1.3762
6	12	2	68.279	4	68.280	−0.001	1.3725
−10	10	3	68.770	1	68.787	−0.017	1.3639
6	6	5	69.106	2	69.103	0.003	1.3581
1	1	7	69.258	2	69.252	0.006	1.3555
2	10	5	69.570	1	69.576	−0.006	1.3501
−6	12	4	69.912	1	69.930	−0.018	1.3444

on a binary join[3] between $Ba_6Fe_{45}Ti_{17}O_{106}$ and the end member of a solid solution of Ti^{4+} in $BaFe_{12}O_{19}$ (i.e., $\sim BaFe_{10.8}Ti_{0.9}O_{19}$) (3). After heating this mixture at 1265°C for 4.5 days under flowing oxygen at 1 atm, followed by cooling at 250°C/h to ambient, the amount of the $BaFe_{12}O_{19}$-type second phase was significantly reduced to just-detectable limits by X-ray diffraction, thus confirming a shift in composition from $Ba_6Fe_{45}Ti_{17}O_{106}$ toward the fully oxidized (i.e., all Fe^{3+}/Ti^{4+}) stoichiometry $Ba_6Fe_{48}Ti_{14}O_{106}$. The chemical formula for this phase can therefore be written as $Ba_6Fe_{48-x}Ti_{14+x}O_{106}$, where $x = 3$ in air and $x = 0$ in 100% oxygen using a synthesis temperature of 1265°C. The value of x corresponds to the equivalents of reduction taking place within the [(Fe,Ti)O_6] octahedra to maintain electroneutrality as the Ti-content of the phase increases. Higher values of x may be achievable at lower oxygen partial pressures.

The crystal structure reported here for $Ba_6Fe_{45}Ti_{17}O_{106}$ is similar to that reported by Adams *et al.* (6) for a phase with the nominal composition $Ba_6Fe_{48}Ti_{14}O_{106}$ ($= Ba_6Fe_{48-x}Ti_{14+x}O_{106}$ with $x = 0$). Although the details of sample preparation are not given, the authors report that

[3] This point actually falls just inside a three-phase field with a minimum trace (by X-ray diffraction) of another new compound near the stoichiometry $Ba_2Fe_{12}Ti_3O_{26}$ (phase "F" in (3), and mislabeled there as "1:6:3" instead of "2:6:3" $BaO:Fe_2O_3:TiO_2$). Detailed structural studies and property measurements of this phase are in progress and will be described elsewhere.

TABLE 5
Bond Distances (Å), Average Bond Distance (Å), Site Distortion Ratio (Defined as the Ratio of the Shortest to the Longest Bond Distance), and Bond Valence Sum (BVS; v.u)[a] about Each of the Cation Sites in $Ba_6Fe_{45}Ti_{17}O_{106}$

Ba1–O1	2.80(2) x2	–O28	2.09(2)	–O17	1.95(2)	**M9**–O1	1.91(2)	–O23	2.12(2)	**M16**–O9	1.90(2)
–O6	2.90(2) x2	–O30	2.23(1)	–O20	1.85(2)	–O6	2.06(2)	–O33	2.14(2)	–O23	1.91(2)
–O7	2.80(2) x2	*average:*	*2.05*	–O26	2.06(2)	–O10	1.90(2)	*average:*	*2.00*	–O25	1.99(2)
–O8	2.88(2) x2	*distortion*	*0.83*	–O32	2.04(2	–O18	2.10(2)	*distortion*	*0.90*	–O26	2.28(2)
–O11	2.96(2) x2	BVS_{obs}	*3.18*	*average:*	*1.99*	–O23	2.01(2)	BVS_{obs}	*3.27*	–O32	1.97(2)
–O13	3.05(2)	BVS_{calc}	*3.42*	*distortion*	*0.90*	–O26	2.16(2)	BVS_{calc}	*3.20*	–O33	1.89(2)
–O30	3.02(2)			BVS_{obs}	*3.44*	*average:*	*2.02*			*average:*	*1.99*
average:	*2.90*	**M2**–O1	1.94(2)	BVS_{calc}	*3.42*	*distortion*	*0.88*	**M13**–O10	1.86(2)	*distortion*	*0.83*
distortion	*0.92*	–O4	2.04(2)			BVS_{obs}	*3.09*	–O11	1.94(2)	BVS_{obs}	*3.51*
BVS_{obs}	*2.38*	–O11	1.99(2)	**M6**–O10	1.97(2)	BVS_{calc}	*3.10*	–O14	1.94(2)	BVS_{calc}	*3.23*
		–O12	2.22(2)	–O18	1.94(2)			–O24	1.99(2)		
Ba2–O3	2.95(2)	–O13	2.08(1)	–O18	2.15(2)	**M10**–O6	1.93(2)	–O27	2.11(2)	**M17**–O5	2.18(2) x2
–O5	2.94(2) x2	–O14	1.98(2)	–O19	1.95(2)	–O7	2.10(2)	–O29	2.10(2)	–O14	1.93(2) x2
–O16	3.02(3)	*average:*	*2.04*	–O23	2.05(2)	–O9	1.95(2)	*average:*	*1.99*	–O15	2.22(2)
–O17	2.94(2) x2	*distortion*	*0.87*	–O25	1.98(2)	–O17	2.06(2)	*distortion*	*0.88*	–O16	1.96(2
–O20	3.07(2) x2	BVS_{obs}	*2.92*	*average:*	*2.01*	–O26	2.06(2)	BVS_{obs}	*3.53*	*average:*	*2.07*
–O28	2.87(2) x2	BVS_{calc}	*3.17*	*distortion*	*0.90*	–O26	2.21(2)	BVS_{calc}	*3.45*	*distortion*	*0.87*
–O32	2.97(2) x2			BVS_{obs}	*3.19*	*average:*	*2.05*			BVS_{obs}	*3.02*
average:	*2.96*	**M3**–O3	2.08(2)	BVS_{calc}	*3.16*	*distortion*	*0.87*	**M14**–O2	2.29(1)	BVS_{calc}	*3.60*
distortion	*0.93*	–O21	2.29(2) x2			BVS_{obs}	*2.82*	–O21	2.01(2) x2		
BVS_{obs}	*1.96*	–O31	1.91(1)	**M7**–O4	1.99(3)	BVS_{calc}	*3.06*	–O22	1.83(2)	**M18**–O7	1.88(2)
		–O33	1.90(2) x2	–O12	2.00(2)			–O28	1.97(2) x2	–O8	1.90(2)
Ba3–O8	2.95(2) x2	*average:*	*2.06*	–O13	2.06(2) x2	**M11**–O11	2.18(2)	*average:*	*2.01*	–O11	2.20(2)
–O19	2.94(2) x2	*distortion*	*0.83*	–O20	1.92(2) x2	–O12	2.06(2)	*distortion*	*0.80*	–O24	2.08(2)
–O21	3.06(2) x2	BVS_{obs}	*3.22*	*average:*	*1.99*	–O16	1.94(2)	BVS_{obs}	*3.51*	–O25	1.95(2)
–O25	2.90(2) x2	BVS_{calc}	*3.62*	*distortion*	*0.93*	–O20	2.05(2)	BVS_{calc}	*3.60*	–O29	2.21(1)
–O29	2.89(3)			BVS_{obs}	*3.35*	–O24	2.06(2)			*average:*	*2.04*
–O31	2.86(3)	**Fe4**–O4	1.91(3)	BVS_{calc}	*3.23*	–O27	2.04(1)	**M15**–O2	2.24(1)	*distortion*	*0.85*
–O33	2.86(2) x2	–O15	1.98(2)			*average:*	*2.06*	–O3	1.94(2)	BVS_{obs}	*3.24*
average:	*2.93*	–O32	1.86(2) x2	**Fe8**–O5	1.83(2)	*distortion*	*0.89*	–O9	1.88(2)	BVS_{calc}	*3.47*
distortion	*0.93*	*average:*	*1.90*	–O17	1.82(2)	BVS_{obs}	*2.95*	–O21	1.91(2)		
BVS_{obs}	*2.13*	*distortion*	*0.94*	–O18	1.88(2)	BVS_{calc}	*3.47*	–O28	1.93(2)		
		BVS_{obs}	*2.73*	–O24	1.90(2)			–O30	1.99(2)		
M1–O6	1.89(2)	BVS_{calc}	*3.00*	*average:*	*1.86*	**M12**–O5	1.93(2)	*average:*	*1.98*		
–O8	1.87(2)			*distortion*	*0.96*	–O15	1.94(2)	*distortion*	*0.84*		
–O19	1.96(2)	**M5**–O1	2.03(2)	BVS_{obs}	*3.07*	–O19	1.93(2)	BVS_{obs}	*3.64*		
–O21	2.24(2)	–O7	2.03(2)	BVS_{calc}	*3.00*	–O22	1.96(2)	BVS_{calc}	*3.40*		

Note. Six-coordinated *M* sites are initially assumed here to contain a mixture of Fe^{3+} and Ti^{4+}.

[a] The BVS_{obs} values given for the mixed six-coordinated *M* sites were calculated from the observed bond distances using the (Fe^{3+};Ti^{4+}) parameters (i.e., 1.759;1.815, respectively (28)) and the Fe/Ti occupancies indicated by neutron powder diffraction (Table 3). The BVS_{calc} value for each site was calculated from the Fe/Ti occupancies in Table 3 and the initially assumed formal valences of 3+ for Fe and 4+ for Ti.

a stoichiometric composition was heated at 1375°C for 48 h to obtain crystals that were analyzed by single-crystal X-ray diffraction. The unit cell and space group obtained are essentially the same as those given here and earlier (3) for $Ba_6Fe_{45}Ti_{17}O_{106}$; however, the positional parameters and polyhedral arrangements within some of the layers are slightly different. The present results indicate that the composition reported in Ref. (6), $Ba_6Fe_{48}Ti_{14}O_{106}$, was incorrectly deduced by assuming the oxidation states of Fe^{3+} and Ti^{4+}; the crystals described are most likely $Ba_6Fe_{45}Ti_{17}O_{106}$, the same composition as that described here.

2. *Magnetic Properties of $Ba_6Fe_{45}Ti_{17}O_{106}$*

The field dependence of the magnetization of $Ba_6Fe_{45}Ti_{17}O_{106}$ measured at 5, 300, and 1073 K is shown in Fig. 4. The curves are predominantly linear, with susceptibilities (χ) of 6.2×10^{-7}, 3.1×10^{-7}, and 1.8×10^{-7} m^3/kg, respectively, indicating primarily paramagnetic behavior. At 5 and 300 K, a small ferromagnetic (or ferrimagnetic) component is observed which saturates at low fields and exhibits a coercivity that increases with decreasing temperature. As seen in Fig. 5, the magnetization vs temperature data above 300 K indicate essential coincidence of the field-cooling and zero-field-cooling data; the susceptibility of the sample decreases with increasing temperature, and no discontinuities suggesting magnetic phase transitions are observed. In addition, the $1/\chi$ vs T curve, also shown in Fig. 5, follows the Curie–Weiss law at high temperatures, as expected for a paramagnet. The observation of paramagnetism for $Ba_6Fe_{45}Ti_{17}O_{106}$ near room temperature is surprising given the high Fe-content of this phase (26%). Structurally similar neighboring phases (3) with comparable Fe-content, such as $Ba_{12}Fe_{28}Ti_{15}O_{84}$ (37) and $BaFe_{12}O_{19}$, exhibit Curie temperatures significantly higher than room temperature. The paramagnetic behavior of $Ba_6Fe_{45}Ti_{17}O_{106}$ may be partially explained by the large negative extrapolated intercept (-806 K) of the $1/\chi$ vs T high-temperature data (Fig. 5), which indicates the existence of strong antiferromagnetic interactions between magnetic species. The effective moment calculated from the slope (3.3×10^3 kg/m^3K) of the Curie–Weiss behavior yields an

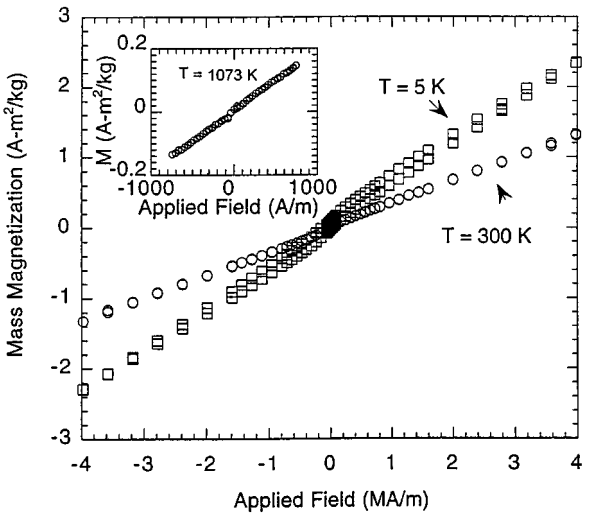

FIG. 4. Field dependence of the magnetization for $Ba_6Fe_{45}Ti_{17}O_{106}$ measured at 5, 300, and 1073 K (inset). The curves are predominantly linear, with susceptibilities (χ) of 6.2×10^{-7}, 3.1×10^{-7}, and 1.8×10^{-7} m^3/kg, respectively, indicating primarily paramagnetic behavior. Slight hysteresis is observed in the 5 K data, which probably arises from a small amount ($< 0.5\%$) of a highly magnetic impurity phase.

unusually low value of 34 μ_B per mole $Ba_6Fe_{45}Ti_{17}O_{106}$. Assuming the valence configuration $Ba_6Fe^{2+}{}_3Fe^{3+}{}_{42}Ti^{4+}{}_{17}O_{106}$ (Fe^{2+}: d^6, high-spin $S = 2$; Fe^{3+}: d^5, high-spin $S = 5/2$), the calculated spin-only moment is 263 μ_B per mole compound, which is nearly an order of magnitude larger than the effective moment indicated by the paramagnetic Curie–Weiss behavior.

Below room temperature, as shown in Fig. 6, the magnetic behavior of $Ba_6Fe_{45}Ti_{17}O_{106}$ remains predominantly paramagnetic, with the susceptibility continuing to increase with decreasing temperature down to 5 K. However, as in Fig. 4, a small amount ($<0.5\%$) of some ferromagnetic (or ferrimagnetic) component is also observed which exhibits a coercivity that increases with decreasing temperature, as expected for thermally assisted domain kinetics. The difference between the FC and ZFC data at the lower fields in Fig. 6 most likely arises because the coercivity of the ferromagnetic component in those temperature regions is larger than the measuring and cooling field. Similarly, the peak in the lowest field data near 100 K occurs because below that temperature the coercivity becomes larger than the measuring field (7.96 kA/m (100 Oe)) and the ferromagnetic contribution consequently becomes smaller. The identity of the ferromagnetic impurity is not known; however, $Ba_6Fe_{45}Ti_{17}O_{106}$ occurs in equilibrium (3) with a highly ferromagnetic $BaFe_{12}O_{19}$-type solid solution ($\sim BaFe_{10.8}Ti_{0.9}O_{19}$), the presence of which would not be detectable by diffraction methods at levels $\leq 1\%$. As shown in the magnified inset to Fig. 6, a small discontinuity in the magnetic susceptibility of $Ba_6Fe_{45}Ti_{17}O_{106}$ is observed just below room temperature, near 280 K. This discontinuity persisted in measuring fields as high as 40 MA/m, and was

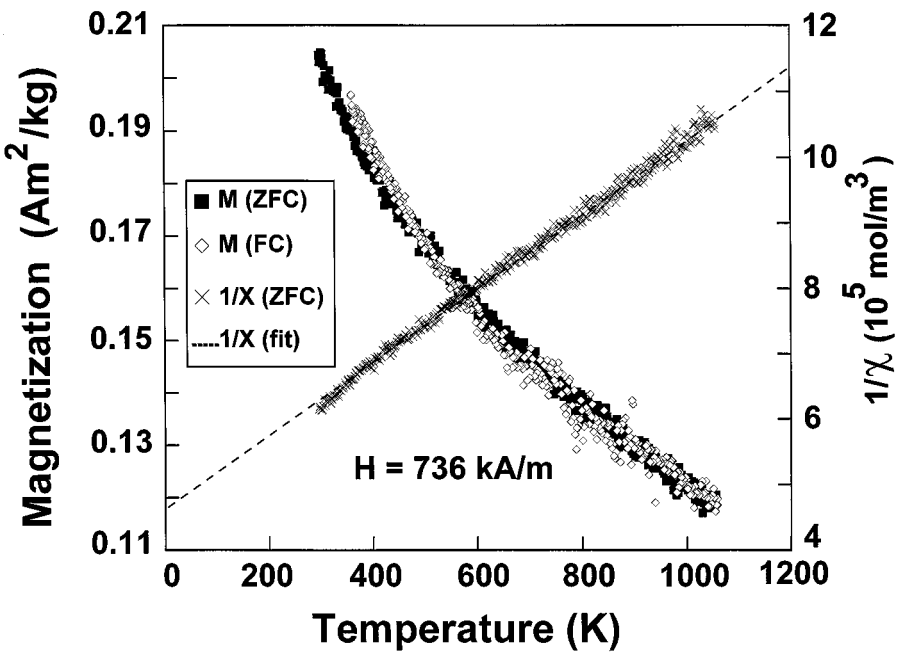

FIG. 5. High-temperature magnetic behavior of $Ba_6Fe_{45}Ti_{17}O_{106}$: Magnetization and inverse mass susceptibility ($1/\chi$) from 300 to 1073 K with an applied field of 736 kA/m (9250 Oe). The field-cooling and zero-field-cooling data are essentially coincident, and no discontinuities suggesting magnetic phase transitions are observed. The inverse susceptibility vs temperature curve indicates antiferromagnetic Curie–Weiss behavior at high temperatures with an effective moment of 34 μ_B per mole $Ba_6Fe_{45}Ti_{17}O_{106}$ and an extrapolated temperature intercept of -806 K.

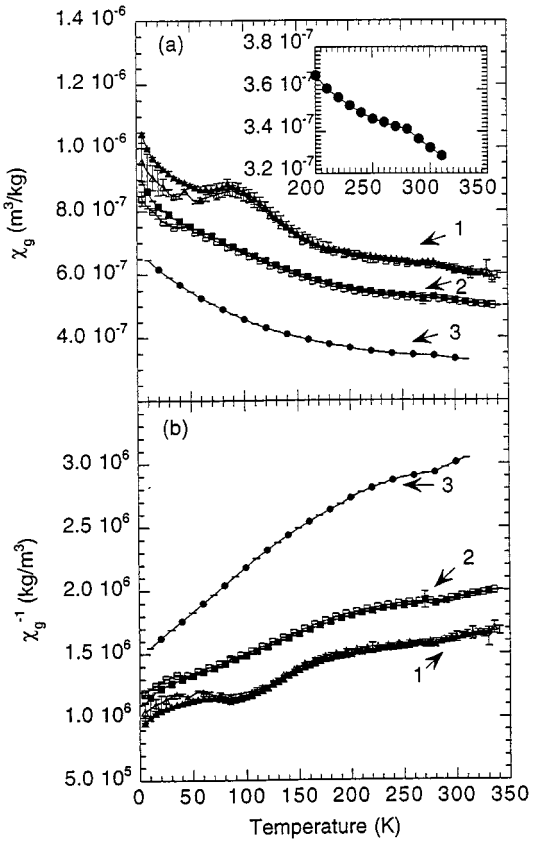

FIG. 6. Low-temperature magnetic behavior of $Ba_6Fe_{45}Ti_{17}O_{106}$: Mass susceptibility and inverse mass susceptibility from 340 to 5 K with applied fields of (1) $H = 8$ kA/m (100 Oe, triangles), (2) 80 kA/m (1000 Oe, squares), and (3) 4 MA/m (50,000 Oe, circles). The $H = 8$ kA/m and 80 kA/m data are also shown for field-cooled (open symbols) and zero-field-cooled (filled symbols) initial conditions. The magnetic transitions below 100 K probably arise from a small amount ($< 0.5\%$) of a highly magnetic impurity phase such as barium hexaferrite. The inset shows magnification of the χ_g vs T behavior near room temperature at high field (4 MA/m). The kink observed near 280 K suggests some type of long-range magnetic ordering phenomenon.

reproducibly obtained from different sample batches and in different laboratories. This observation suggests the existence of some type of long-range magnetic ordering phenomenon near 280 K, the nature of which is not yet understood.

The magnetic behavior observed in the present study for $Ba_6Fe_{45}Ti_{17}O_{106}$ (Figs. 5 and 6) is completely different from that reported by Adams *et al.* for apparently the same phase (6). The mass magnetization values reported in Ref. (6) are two orders of magnitude larger than those observed in the present study at similar applied fields. Furthermore, a marked transition to paramagnetic behavior (Curie point) was observed above 600 K (6), and the magnetization vs applied field hysteresis loops exhibited pronounced plateaus indicative of saturation, in contrast to those obtained here (Fig. 4). These significant discrepancies in the reported magnetic behavior arise because the sample used in (6) was probably a mixture of weakly magnetic $Ba_6Fe_{45}Ti_{17}O_{106}$ and a highly magnetic $BaFe_{12}O_{19}$-type solid solution. To confirm this, the sample preparation reported in (6) was repeated by heating a mixture with the overall composition "$Ba_6Fe_{48}Ti_{14}O_{106}$" (which, as described above, corresponds to a mixture of ≈ 80 mol% $Ba_6Fe_{45}Ti_{17}O_{106}$ and ≈ 20 mol% $BaFe_{10.8}Ti_{0.9}O_{19}$) above the solidus, at 1375°C, for 48 h. A complete melt was obtained under these conditions, and X-ray powder diffraction analysis of a representative portion of the recrystallized reaction mass indicated that the $BaFe_{12}O_{19}$-type solid solution had become the major component, with $Ba_6Fe_{45}Ti_{17}O_{106}$ still present as a minor component ($\sim 30\%$). The composition used to prepare the sample measured in (6) apparently occurs in the primary phase field of the $BaFe_{12}O_{19}$-type phase, and the magnetic properties reported there most likely correspond to a $\approx 70{:}30$ mixture of $BaFe_{12}O_{19}$-type solid solution, saturated with Ti^{4+}, and $Ba_6Fe_{45}Ti_{17}O_{106}$. As pointed out by the authors (6), the magnetic behavior of their sample differed considerably from that of pure $BaFe_{12}O_{19}$; however, this result is expected when Ti^{4+} is substituted for Fe^{3+} in the $BaFe_{12}O_{19}$ structure. To quantify these effects, the magnetic properties of the end member of the Ti^{4+}–$BaFe_{12}O_{19}$ solid solution (i.e., $BaFe_{10.8}Ti_{0.9}O_{19}$, prepared at 1250°C (3)) were measured and are shown in Fig. 7. The nature of the curves and the magnetization values are essentially the same as those reported in (6) and mistakenly

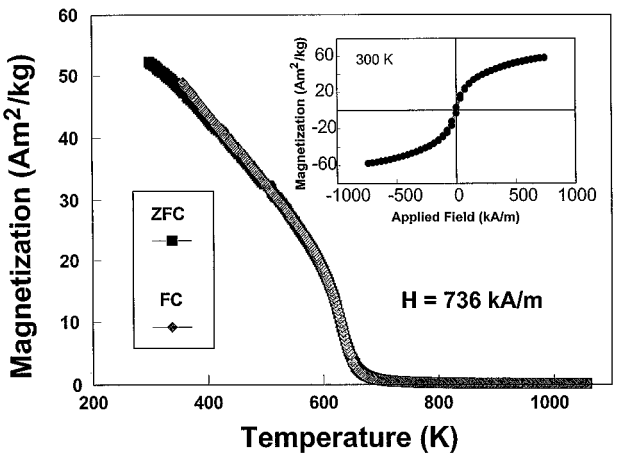

FIG. 7. Magnetization data as a function of temperature and applied field (inset) for $BaFe_{10.8}Ti_{0.9}O_{19}$, which is the end member (at 1250°C, subsolidus) of a $BaFe_{12}O_{19}$-type solid solution. The nature of the curves and the magnetization values are similar to those for undoped $BaFe_{12}O_{19}$. Ti-substitution lowers the Curie temperature of $BaFe_{12}O_{19}$ from ~ 750 to ~ 675 K. As seen by comparison with Figs. 5 and 6, the magnetization of $BaFe_{10.8}Ti_{0.9}O_{19}$ is more than two orders of magnitude larger than that of $Ba_6Fe_{45}Ti_{17}O_{106}$; therefore, the magnetic properties of a mixture of these two compounds (6) will be overwhelmed by the properties of the $BaFe_{12}O_{19}$-type component.

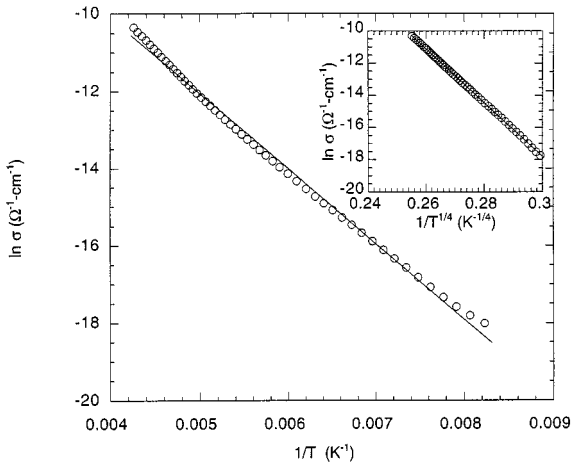

FIG. 8. Conductivity vs inverse temperature data illustrating the nonmetallic behavior of $Ba_6Fe_{45}Ti_{17}O_{106}$. The solid line through the data represents a linear fit assuming thermal activation ($\sigma = \sigma_0 \exp(-\Delta|kT)$) and yields an activation energy $\Delta = 0.17$ eV. An improved fit to the data, as shown in the inset, was obtained using the expression for three-dimensional variable range hopping ($\sigma = \sigma_0 \exp[-(T_0/|T)^{1/4}]$).

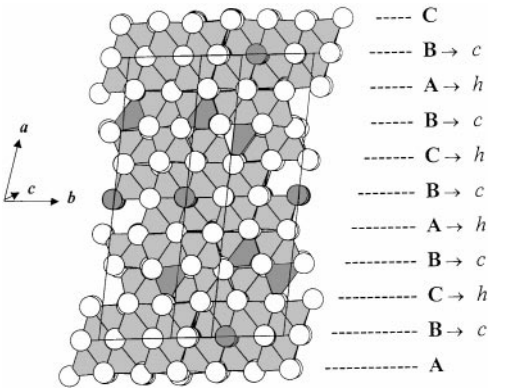

FIG. 9. The structure of $BaFe_{11}Ti_3O_{23}$ as viewed approximately along the c-direction emphasizing the stacking sequence of the close-packed [O,(Ba,O)] layers. The resulting $(ch)_4$ repeat pattern is the same as in $Ba_6Fe_{45}Ti_{17}O_{106}$. Successive layers alternate between *ccp* and *hcp* along the *a*-axis, resulting in an 8L structure with a unit cell metrically similar to that of $Ba_6Fe_{45}Ti_{17}O_{106}$ but with a much shorter *b*-axis. Shaded spheres denote Ba ions, white spheres are oxygens; the darker polyhedra depict $[FeO_4]$ tetrahedra while the lighter polyhedra represent the mixed $[(Fe,Ti)O_6]$ octahedral sites. The structural formula for the compound is $^{XII}Ba\ ^{IV}Fe_2{}^{VI}(Fe_9Ti_3)O_{23}$.

ascribed to "$Ba_6Fe_{48}Ti_{14}O_{106}$" (i.e., $Ba_6Fe_{45}Ti_{17}O_{106}$). As seen in Fig. 7, a Curie temperature near 675 K is indicated for $BaFe_{10.8}Ti_{0.9}O_{19}$, which is in good agreement with other work (38) reporting that the Curie temperature of $BaFe_{12}O_{19}$ is decreased from $\sim$750 to $\sim$685 K with Ti-substitution. The lower value of 600 K reported for the sample used in Ref. (6) suggests that the $BaFe_{12}O_{19}$-type phase measured in that study contained more Ti than the subsolidus end-member $BaFe_{10.8}Ti_{0.9}O_{19}$, a result consistent with the higher preparation temperatures that resulted in a complete melt.

3. *Electrical Properties of $Ba_6Fe_{45}Ti_{17}O_{106}$*

The results of resistivity vs temperature measurements of $Ba_6Fe_{45}Ti_{17}O_{106}$ are given in Fig. 8, in which the conductivity, $\sigma = 1/\rho$, is plotted against inverse temperature. The compound exhibits nonmetallic behavior consistent with thermally activated hopping conductivity. The magnitude of the dc conductivity is several orders of magnitude larger than that observed for polycrystalline $BaFe_{12}O_{19}$ (39,40). The solid line through the data shown in Fig. 8 represents the fit obtained using a simple thermally activated hopping expression, $\sigma = \sigma_0 \exp(-\Delta/kT)$, which yields an activation energy, Δ, of 0.17 eV. An improved fit to the observed data, as seen in the inset to Fig. 8, was obtained using the expression for three-dimensional variable range hopping (vrh), $\sigma = \sigma_0 \exp[-(T_0/T)^{1/4}]$ (41). This type of hopping behavior is expected in systems in which localization is sufficiently weak (compared to the distance between hopping centers) to permit hopping sites that are not necessarily nearest neighbors. These results are consistent with the stoichiometry determined by the structural and phase diagram studies, which indicates slight reduction of the transition metals (three electrons per $Ba_6Fe_{45}Ti_{17}O_{106}$) that would tend to offset localized behavior.

The room-temperature permittivity and dielectric loss tangent values for $Ba_6Fe_{45}Ti_{17}O_{106}$ measured at 347 MHz were 24 and 0.10, respectively. This compound exhibits lossy dielectric behavior, as evidenced by near destruction of the dominant cavity mode upon sample insertion. The dielectric loss is expected to increase with frequency and should be approximately 0.29 at 1 GHz, assuming linearity of the frequency dispersion dependence. The relative permittivity of $Ba_6Fe_{45}Ti_{17}O_{106}$ is comparable in magnitude to values exhibited by other ternary compounds in the BaO–Fe_2O_3–TiO_2 system (4,5,29).

4. *Crystal Chemistry of $BaFe_{11}Ti_3O_{23}$*

The single-crystal X-ray diffraction study confirmed that this compound crystallizes in space group $C2/c$ with the lattice parameters given in Table 1. Since the synthesis of a bulk polycrystalline sample in air was unsuccessful, structural information was only obtainable from the single-crystal X-ray data. Positional parameters and site occupancies are collected in Table 6. The stoichiometry $BaFe_{11}Ti_3O_{23}$ was determined from the refined site occupancies, and should be considered approximate owing to the similar X-ray scattering factors for Fe and Ti.

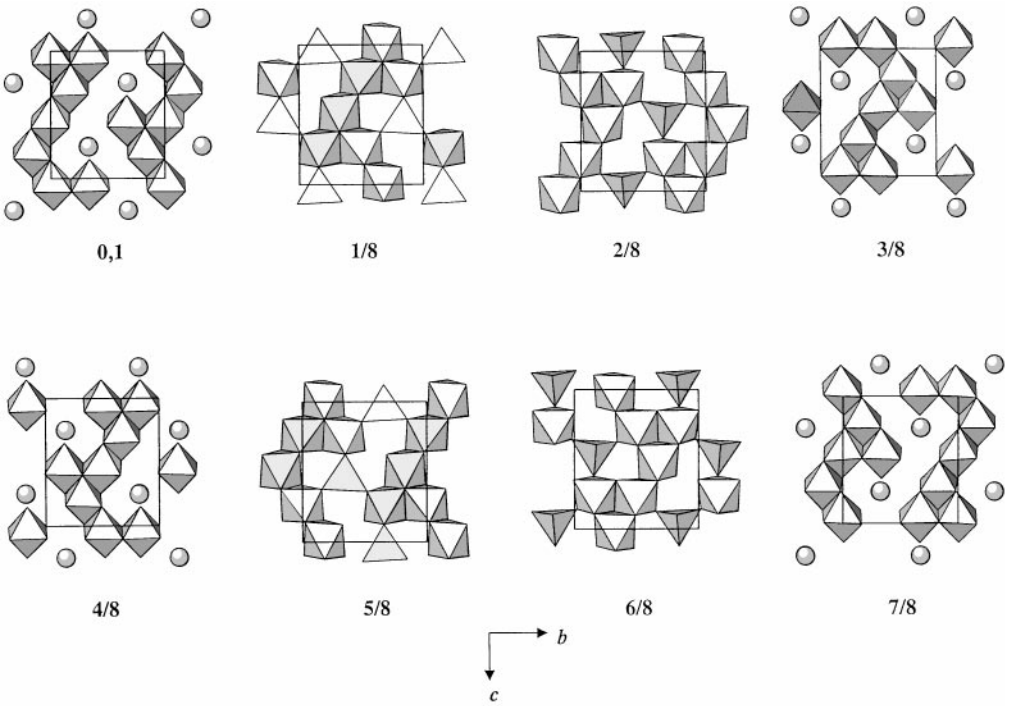

FIG. 10. Views of the polyhedral patterns formed within each of the eight close-packed (*cp*) layers of the $BaFe_{11}Ti_3O_{23}$ structure. The line of sight is perpendicular to the *bc*-plane, which is parallel to the *cp* layers. Spheres denote Ba ions; oxygens are represented as polyhedral vertices. As in $Ba_6Fe_{45}Ti_{17}O_{106}$, $[(Fe,Ti)O_6]$ octahedra share edges within and between the layers. Half of the layers contain edge-sharing $[FeO_4]$ tetrahedra that are vertex-linked to $[(Fe,Ti)O_6]$ octahedra.

The structure of $BaFe_{11}Ti_3O_{23}$ is related to but simpler than that of $Ba_6Fe_{45}Ti_{17}O_{106}$, with a unit cell metrically similar to that of $Ba_6Fe_{45}Ti_{17}O_{106}$ except for the much shorter *b*-axis (Table 1). As shown in Fig. 9, $BaFe_{11}Ti_3O_{23}$ adopts an 8L close-packed structure built from alternating *ccp* and *hcp* [O,(Ba,O)] layers stacked along the *a*-direction with a $(ch)_4$ repeating sequence just as in $Ba_6Fe_{45}Ti_{17}O_{106}$ (Fig. 2). All Ba ions are 12-coordinated and the close-packed array does not contain vacancies. The structure contains tetrahedral sites occupied by Fe^{3+} and octahedral sites occupied by a mixture of Fe and Ti, resulting in the structural formula $^{XII}Ba^{IV}Fe_2{}^{VI}(Fe_9Ti_3)O_{23}$.

The patterns formed by the transition-metal polyhedra within each of the eight *cp* layers in $BaFe_{11}Ti_3O_{23}$ are illustrated in Fig. 10. The distribution of $[FeO_4]$ tetrahedra and Ba within the *cp* layers is considerably different from that in $Ba_6Fe_{45}Ti_{17}O_{106}$; in the structure of $BaFe_{11}Ti_3O_{23}$, half of the layers are seen to be Ba-free. As in $Ba_6Fe_{45}Ti_{17}O_{106}$, within and between layers, the $[(Fe,Ti)O_6]$ octahedra are linked to each other by edges and vertices only, and no face-sharing occurs despite the presence of four *hcp* layers per unit cell. An extraordinary feature in the structure of $BaFe_{11}Ti_3O_{23}$ is the occurrence of pairs of edge-sharing $[FeO_4]$ tetrahedra between the 1/8,2/8 and 5/8,6/8 layers (Fig. 10). The expected cation–cation repulsion effects are manifest in elongated Fe7–O3 bond distances, shown in Fig. 11, with displacement of the Fe^{3+} ions away from the shared O3–O3 edge. As seen in Table 6, the temperature factors obtained for Fe7 are considerably higher than those obtained for the other metals. In a trial refinement allowing the Fe7 occupancy factor to vary from 1.0, an occupancy of 85% was obtained with temperature factors comparable (e.g., $U_{eq} = 0.0076(3)$ Å^2) to those of the other metals. The atomic positions and bond distances obtained from this refinement were negligibly different from those reported in Tables 6 and 7, and both refinements are consistent with the unusual crystal chemistry about the Fe7 site.

Bond distances, site distortion ratios, and bond valence sums (28) for $BaFe_{11}Ti_3O_{23}$ are collected in Table 7. All the polyhedra in the structure are somewhat distorted. The bond valence sum about Fe7 is seen to be somewhat low, which may indicate residual tensile stress related to cation–cation repulsion across the shared tetrahedral edge. In a manner similar to that described above for $Ba_6Fe_{45}Ti_{17}O_{106}$, the bond valence sums for the mixed $[(Fe,Ti)O_6]$ octahedral sites were first calculated from the occupancy-weighted averages assuming the oxidation states of Fe^{3+} and Ti^{4+}. The estimated stoichiometry of the compound, however, requires one equivalent of reduction per $BaFe_{11}Ti_3O_{23}$ formula unit to achieve electroneutrality.

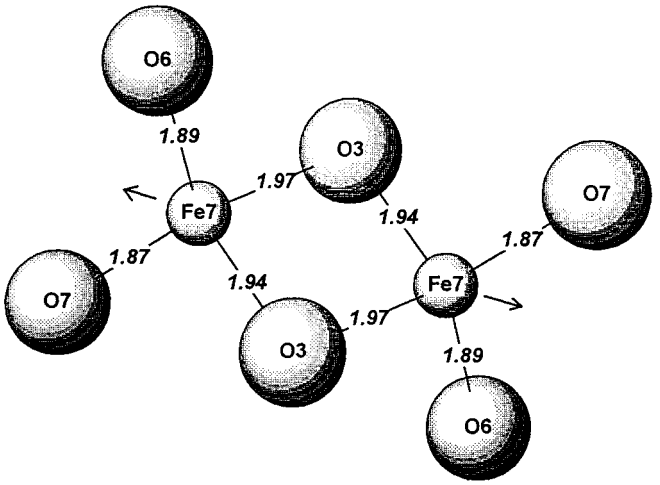

FIG. 11. Local coordination about the tetrahedral Fe7 sites in the $BaFe_{11}Ti_3O_{23}$ structure, with bond distances indicated (Å). The pairs of edge-sharing [FeO_4] tetrahedra occur between the 1/8,2/8 and 5/8,6/8 layers illustrated in Fig. 10. Cation–cation repulsion effects are manifest in elongated Fe7–O3 bond distances, with displacement of the Fe^{3+} ions away from the shared O3–O3 edge. This unusual structural feature is infrequently observed in oxide systems and is likely related to the metastable nature of this compound.

Inspection of Table 7 reveals low observed bond valence sums for sites *M*1 and *M*2 which would be consistent with the presence of larger reduced ions. As was done for $Ba_6Fe_{45}Ti_{17}O_{106}$, recalculation of the bond valence sums about these sites assuming reduction to Fe^{2+} (or Ti^{3+}) resulted in better agreement between observed and calculated bond valence sums, and calculation of the total equivalents of reduction from the site multiplicities yielded a sum near that required for electroneutrality of the unit cell contents.

$BaFe_{11}Ti_3O_{23}$ is apparently a metastable phase in air below the solidus and likely crystallized as a minor coproduct under reduced pO_2 conditions within the melt during the growth of $Ba_6Fe_{45}Ti_{17}O_{106}$ crystals. The extent of reduction on the mixed Fe/Ti sites is somewhat higher in $BaFe_{11}Ti_3O_{23}$ (8.3 at% vs 5.4 at% in $Ba_6Fe_{45}Ti_{17}O_{106}$). In air at 1250–1275°C, this composition is found to be a two-phase mixture occurring on the join between $Ba_6Fe_{45}Ti_{17}O_{106}$ and Ti-saturated hematite (3). In an attempt to prepare bulk $BaFe_{11}Ti_3O_{23}$, a specimen of this composition was heated in the solid state at 1350°C in a 90/10 N_2/O_2 atmosphere at ambient pressure, yielding a product unchanged from the starting two-phase mixture. When heated at lower pO_2 in a CO/CO_2 mixture, the $Ba_6Fe_{45}Ti_{17}O_{106}$-type phase decomposed and the products were ilmenite plus a reduced form of a $BaFe_{12}O_{19}$-type solid solution. The occurrence of edge-sharing tetrahedra, as has been found in $BaFe_{11}Ti_3O_{23}$, is infrequently observed in oxides (42), and is likely related to the metastable nature of this compound in spite of the fact that its crystal structure is considerably simpler than that of $Ba_6Fe_{45}Ti_{17}O_{106}$. This unusual structural feature suggests that the deliberate preparation of $BaFe_{11}Ti_3O_{23}$ may be difficult under any conditions.

TABLE 6
Refined Coordinates, Fe/Ti Site Occupancies, and Thermal Parameters for $BaFe_{11}Ti_3O_{23}$ as Determined by Single-Crystal X-Ray Diffraction

Atom	Site	*x*	*y*	*z*	Fe_{occ}/Ti_{occ}	U_{11}(Å^2)	U_{22}(Å^2)	U_{33}(Å^2)	U_{23}(Å^2)	U_{13}(Å^2)	U_{12}(Å^2)	U_{eq}(Å^2)
Ba	4*e*	0.0	0.32589(6)	0.25		0.0046(2)	0.0150(3)	0.0093(2)	0.0000(0)	0.0037(2)	0.0000(0)	0.0093(2)
*M*1	8*f*	0.06483(5)	0.0064(1)	0.44697(9)	0.65(2)/0.35(2)	0.0063(4)	0.0060(4)	0.0074(4)	−0.0005(3)	0.0034(3)	−0.0008(3)	0.0062(2)
*M*2	8*f*	−0.06677(5)	0.6368(1)	0.03491(9)	0.72(3)/0.28(3)	0.0051(4)	0.0060(4)	0.0068(4)	−0.0003(3)	0.0034(3)	0.0007(3)	0.0056(2)
*M*3	8*f*	−0.06724(5)	0.8182(1)	0.30542(9)	0.63(3)/0.37(3)	0.0046(4)	0.0075(4)	0.0073(4)	−0.0004(3)	0.0025(3)	−0.0006(3)	0.0063(2)
*M*4	8*f*	0.31749(4)	0.0009(1)	0.22908(8)	0.91(3)/0.09(3)	0.0044(4)	0.0053(4)	0.0062(4)	−0.0008(3)	0.0022(3)	0.0002(3)	0.0051(2)
*M*5	8*f*	0.17535(5)	0.1533(1)	0.24214(9)	0.77(3)/0.23(3)	0.0030(4)	0.0048(4)	0.0070(4)	0.0003(3)	0.0014(3)	0.0000(3)	0.0049(2)
*M*6	8*f*	0.18065(4)	0.3123(1)	0.51944(8)	0.84(3)/0.16(3)	0.0027(4)	0.0083(4)	0.0048(4)	−0.0010(3)	0.0020(3)	−0.0003(3)	0.0051(2)
Fe7	8*f*	0.28509(5)	0.3493(1)	0.0746(1)	1.0/0.0	0.0105(4)	0.0140(4)	0.0149(4)	0.0029(3)	0.0071(3)	0.0039(3)	0.0124(2)
O1	8*f*	0.2370(2)	0.3234(5)	0.3768(4)								0.0051(7)
O2	8*f*	0.1254(2)	0.1586(5)	0.3944(4)								0.0067(7)
O3	8*f*	0.2453(2)	0.1553(5)	0.1242(4)								0.0059(7)
O4	8*f*	−0.1307(2)	0.6705(5)	0.3424(4)								0.0062(7)
O5	8*f*	−0.1257(2)	0.4902(5)	0.0961(4)								0.0058(7)
O6	8*f*	−0.1160(2)	0.8234(5)	0.1043(4)								0.0046(7)
O7	8*f*	0.2540(2)	0.0204(5)	0.3588(4)								0.0062(7)
O8	8*f*	0.1242(2)	0.3349(5)	0.1516(4)								0.0053(7)
O9	8*f*	0.0010(2)	0.1666(5)	0.5099(4)								0.0073(7)
O10	4*e*	0.0	0.6693(7)	0.25								0.008(1)
O11	4*e*	0.0	−0.0176(7)	0.25								0.007(1)
O12	4b	0.0	0.5	0.5								0.008(1)
O13	8*f*	0.1191(2)	0.0071(5)	0.649(4)								0.0068(7)

Note. *M* denotes a six-coordinated site with mixed Fe/Ti occupancy. Fe sites are four-coordinated.

TABLE 7
Bond Distances (Å), Average Bond Distance (Å), Site Distortion Ratio (Defined as the Ratio of the Shortest to the Longest Bond Distance), and Bond Valence Sum (BVS; v.u)[a] about Each of the Cation Sites in $BaFe_{11}Ti_3O_{23}$

Ba-O2	2.884(4) x2	**M2**-O5	1.925(4)	**M4**-O1	2.008(4)	**M6**-O1	2.041(4)
-O5	2.904(4) x2	-O6	2.097(4)	-O3	2.025(4)	-O1	2.042(4)
-O8	2.864(4) x2	-O8	1.934(4)	-O4	1.968(4)	-O2	1.951(4)
-O9	2.966(4) x2	-O9	2.214(5)	-O5	1.965(4)	-O4	1.915(4)
-O10	2.974(6) x2	-O10	2.234(1)	-O7	2.042(4)	-O5	2.055(4)
-O11	2.975(6)	-O12	1.866(1)	-O8	2.021(4)	-O7	2.098(4)
-O12	2.945(0)	*average:*	*2.045*	*average:*	*2.005*	*average:*	*2.017*
average:	*2.923*	*distortion*	*0.84*	*distortion*	*0.96*	*distortion*	*0.91*
distortion	*0.96*	BVS_{obs}	*3.11*	BVS_{obs}	*3.14*	BVS_{obs}	*3.11*
BVS_{obs}	*2.18*	BVS_{calc}	*3.28*	BVS_{calc}	*3.09*	BVS_{calc}	*3.16*
M1-O2	1.940(4)	**M3**-O4	1.889(4)	**M5**-O1	2.144(4)	**Fe7**-O3	1.939(4)
-O6	2.017(4)	-O6	2.002(4)	-O2	2.036(4)	-O3	1.972(4)
-O9	2.078(4)	-O9	1.971(4)	-O3	2.044(4)	-O6	1.889(4)
-O9	2.097(4)	-O10	2.026(4)	-O7	2.027(4)	-O7	1.875(4)
-O11	2.065(1)	-O11	2.113(4)	-O8	1.955(4)	*average:*	*1.919*
-O13	2.034(4)	-O13	1.945(4)	-O13	1.863(4)	*distortion*	*0.95*
average:	*2.038*	*average:*	*1.991*	*average:*	*2.012*	BVS_{obs}	*2.61*
distortion	*0.92*	*distortion*	*0.89*	*distortion*	*0.87*	BVS_{calc}	*3.00*
BVS_{obs}	*3.01*	BVS_{obs}	*3.46*	BVS_{obs}	*3.44*		
BVS_{calc}	*3.35*	BVS_{calc}	*3.37*	BVS_{calc}	*3.42*		

Note. Six-coordinated *M* sites are initially assumed here to contain a mixture of Fe^{3+} and Ti^{4+}.

[a] The BVS_{obs} values given for the mixed six-coordinated *M* sites were calculated from the observed bond distances using the (Fe^{3+};Ti^{4+}) parameters (i.e., 1.759;1.815 respectively (28)) and the Fe/Ti occupancies estimated by single-crystal X-ray diffraction (Table 6). The BVS_{calc} value for each site was calculated from the Fe/Ti occupancies and the initially assumed formal valences of 3+ for Fe and 4+ for Ti.

CONCLUSION

The structures of $Ba_6Fe_{45}Ti_{17}O_{106}$ and $BaFe_{11}Ti_3O_{23}$, which cocrystallized from a slowly cooled off-stoichiometric melt, have been solved using single-crystal X-ray diffraction methods. Further structural details for $Ba_6Fe_{45}Ti_{17}O_{106}$, including accurate Fe/Ti occupancies, were obtained from a combined refinement using neutron and synchrotron powder diffraction data. The crystal structures and monoclinic unit cells of $Ba_6Fe_{45}Ti_{17}O_{106}$ and $BaFe_{11}Ti_3O_{23}$ are related. Both compounds exhibit 8L close-packed structures built from alternating *ccp* and *hcp* [O,(Ba,O)] layers stacked along the *a*-direction with a $(ch)_4$ repeat sequence. Both structures feature octahedral sites occupied by a mixture of Fe and Ti as well as tetrahedral sites occupied by Fe^{3+}; the structural formulas are $^{XII}Ba_6\ ^{IV}Fe_6\ ^{IV}(Fe_{39}Ti_{17})O_{106}$ and $^{XII}Ba\ ^{IV}Fe_2\ ^{VI}(Fe_9Ti_3)O_{23}$. The structures differ considerably in the distribution of $[FeO_4]$ tetrahedra and Ba within the *cp* layers. An extraordinary feature in the structure of $BaFe_{11}Ti_3O_{23}$ is the occurrence of pairs of edge-sharing $[FeO_4]$ tetrahedral sites. This phase is apparently metastable in air when cooled from above the solidus and likely crystallized as a minor coproduct under reduced pO_2 conditions within the melt; at no time was it observed in the subsolidus $BaO{:}Fe_2O_3{:}TiO_2$ system investigated previously in air (3). $Ba_6Fe_{45}Ti_{17}O_{106}$ and $BaFe_{11}Ti_3O_{23}$ both contain slightly reduced Fe^{3+}/Ti^{4+} arrays; the partial reduction of Fe^{3+} to Fe^{2+} is considered more likely than Ti^{4+} to Ti^{3+}. The bond valence signatures of larger reduced ions were detectable in some of the mixed Fe/Ti octahedral sites in both structures, and hence the extra carriers in both cases appear to be localized.

$Ba_6Fe_{45}Ti_{17}O_{106}$ exhibits variable stoichiometry, $Ba_6Fe_{48-x}Ti_{14+x}O_{106}$, with an Fe:Ti ratio dependent upon the partial pressure of oxygen. Previous reports describing this compound as occurring in air at the stoichiometry $Ba_3Fe_{24}Ti_7O_{53}$ ($=Ba_6Fe_{48}Ti_{14}O_{106}$) are incorrect (3,6). When prepared in air, this phase occurs at $x = 3$ with the stoichiometry $Ba_6Fe_{45}Ti_{17}O_{106}$, while in 1 atm oxygen the *x*-value approaches zero with the resulting stoichiometry $Ba_6Fe_{48}Ti_{14}O_{106}$ (all Fe^{3+} and Ti^{4+}). The value of *x* equals the equivalents of reduction that must occur to maintain electroneutrality as the Ti-content of the phase increases. Higher values of *x* and hence Ti-content should be achievable using lower-pO_2 synthetic conditions. $Ba_6Fe_{45}Ti_{17}O_{106}$ exhibits essentially paramagnetic behavior that obeys the Curie–Weiss law above room temperature. The low effective magnetic moment and the large negative temperature intercept deduced from the Curie Weiss behavior suggest that antiferromagnetic interactions dominate the magnetic behavior of this compound. Resistivity vs temperature measurements of $Ba_6Fe_{45}Ti_{17}O_{106}$ indicated non-metallic behavior and an activation energy on the order of 0.17 eV. Statistical fits of the conductivity vs $1/T$ data suggested a three-dimensional variable range hopping mechanism with hopping sites that are not necessarily nearest neighbors. These results are consistent with the large

dielectric loss tangent (0.10) obtained for $Ba_6Fe_{45}Ti_{17}O_{106}$ at 347 MHz; the value obtained for the permittivity at this frequency was 24. The temperature dependence of the conductivity and the high dielectric loss are both consistent with the partially reduced nature of $Ba_6Fe_{45}Ti_{17}O_{106}$.

ACKNOWLEDGMENTS

The authors are grateful for the technical support provided by J. M. Loezos, L. P. Cook, R. S. Gates, R. Drew, H. R. Brown, C. Li, and A. J. Shapiro.

REFERENCES

1. G. Geiger, *Am. Ceram. Soc. Bull.* **73**(8), 57 (1994).
2. T. Abraham, *Am. Ceram. Soc. Bull.* **73**(8), 62 (1994).
3. T. A. Vanderah, J. M. Loezos, and R. S. Roth, *J. Solid State Chem.* **121,** 38 (1996).
4. T. A. Vanderah, W. Wong-Ng, Q. Huang, R. S. Roth, R. G. Geyer, and R. B. Goldfarb, *J. Phys. Chem. Solids* **58**(9), 1403 (1997).
5. T. A. Vanderah, Q. Huang, W. Wong-Ng, B. C. Chakoumakos, R. B. Goldfarb, R. G. Geyer, J. Baker-Jarvis, R. S. Roth, and A. Santoro, *J. Solid State Chem.* **120,** 121 (1995).
6. R. D. Adams, R. Layland, and C. Payen, *Chem. Ber.* **129,** 1441 (1996).
7. C. R. Hubbard, Y. Zhang, and R. L. McKenzie, Certificate of Analysis, SRM 660, National Institute of Standards and Technology, Gaithersburg, MD, 1989.
8. C. K. Lowe-Ma, Program CELLSVD, Naval Air Warfare Center Weapons Division Technical Publication 8128, Sept. 1993.
9. A. C. Larson and R. B. Von Dreele, GSAS—General Structure Analysis System, 1994.
10. "CAD4 Operations Manual." Enraf-Nonius, Delft, The Netherlands, 1977.
11. G. M. Sheldrick, SHELXLT/PC Version 5, Siemens Analytical X-ray Instruments, Inc., Madison, WI, 1995.
12. E. N. Maflen, A. G. Fox, and M. A. O'Keefe, "International Tables for Crystallography", (A. J. C. Wilson, Ed.), Vol. C, Table 6.1.1.4. Kluwer Academic, Boston, 1992.
13. MOLEN, structure solution package, Enraf-Nonius, Delft, The Netherlands.
14. R. D. Shannon, *Acta Crystallogr. Sect. A* **32,** 751 (1976).
15. L. W. Finger, D. E. Cox, and A. P. Jephcoat, *J. Appl. Crystallogr.* **27,** 892 (1994).
16. L. Hartshorn and W. H. Ward, *J. IEE* **79,** 597 (1936).
17. C. N. Works, T. W. Dakin, and F. W. Boggs, *AIEE Trans.* **63,** 1092 (1944).
18. R. D. Harrington, R. C. Powell, and P. H. Haas, *J. Res. NBS* **56**(3), 129 (1956).
19. A. Kaczkowski and A. Milewski, *IEEE Trans. Microwave Theory Tech.* **MTT-28**(3), 225 (1980).
20. W. Xi, W. R. Tinga, W. A. G. Voss, and B. Q. Tian, *IEEE Trans. Microwave Theory Tech.* **40**(4), 747 (1992).
21. R. G. Geyer, J. Mantese, and J. Baker-Jarvis, NIST Tech. Note 1371, 1994.
22. R. G. Geyer, J. Baker-Jarvis, T. A. Vanderah, and J. Mantese, *Amer. Cer. Soc. Trans.* **88,** (1998).
23. For a discussion of this terminology see A. F. Wells, "Structural Inorganic Chemistry," 5th ed., p. 156. Clarendon Press, Oxford, 1984.
24. E. Tillmans and W. H. Baur, *Acta Crystallogr. Sect.* **B26,** 1645 (1970).
25. E. Tillmans, W. Hofmeister, and W. H. Baur, *J. Solid State Chem.* **58**(1), 14 (1985).
26. R. S. Roth, C. J. Rawn, C. G. Lindsay, and W. Wong-Ng, *J. Solid State Chem.* **104**, 99 (1993).
27. G. S. Smith and R. L. Snyder, *J. Appl. Crystallogr.* **12,** 60 (1979).
28. N. E. Brese and M. O'Keeffe, *Acta Crystallogr. Sect. B* **47,** 192 (1991).
29. T. Siegrist, T. A. Vanderah, A. P. Ramirez, R. G. Geyer, and R. S. Roth, submitted fpr publication
30. I. D. Brown, *J. Solid State Chem.* **82,** 122 (1989).
31. I. D. Brown, *Acta Crystallogr. Sect. B* **48,** 553 (1992).
32. I. D. Brown, *Z. Kristallogr.* **199,** 255 (1992).
33. J. L. García-Muñoz and J. Rodríguez-Carvajal, *J. Solid State Chem.* **115,** 324 (1995).
34. D. G. Peters, J. M. Hayes, and G. M. Hieftje, "Chemical Separations and Measurements," p. A-18. Saunders, Philadelphia, 1974.
35. B. Simons and E. Woermann, *Contrib. Mineral. Petrol.* **66,** 81 (1978).
36. I.E. Grey, A. F. Reid, and D. G. Jones, *Trans. Inst. Mining Met.* **83,** 105 (1974).
37. I. E. Grey, A. Collomb, and X. Obradors, *J. Solid State Chem.* **91,** 131 (1991).
38. G. Heimke, *J. Appl. Phys.* **31**(5), 271S (1960).
39. J. J. Went, G. W. Rathenau, E. W. Gorter, and G. W. van Oosterhaut, *Philips Tech. Rev.* **13,** 194 (1951/1952).
40. F. Haberey and H.P.J. Wijn, *Phys. Status Solidi* **23,** 231 (1968).
41. N. F. Mott and E. A. Davis, "Electronic Processes in Non-crystalline Materials," p. 32. Clarendon Press, Oxford, 1979.
42. A. F. Wells, "Structural Inorganic Chemistry," 5th ed., p. 164. Clarendon Press, Oxford, 1984.